

Pareto Optimization to Accelerate Multi-Objective Virtual Screening

Jenna C. Fromer,[†] David E. Graff,^{†,‡} and Connor W. Coley^{*,†,¶}

[†]*Department of Chemical Engineering, MIT, Cambridge, MA 02139*

[‡]*Department of Chemistry and Chemical Biology, Harvard University, Cambridge, MA*

02138

[¶]*Department of Electrical Engineering and Computer Science, MIT, Cambridge, MA 02139*

E-mail: ccoley@mit.edu

Abstract

The discovery of therapeutic molecules is fundamentally a multi-objective optimization problem. One formulation of the problem is to identify molecules that simultaneously exhibit strong binding affinity for a target protein, minimal off-target interactions, and suitable pharmacokinetic properties. Inspired by prior work that uses active learning to accelerate the identification of strong binders, we implement multi-objective Bayesian optimization to reduce the computational cost of multi-property virtual screening and apply it to the identification of ligands predicted to be selective based on docking scores to on- and off-targets. We demonstrate the superiority of Pareto optimization over scalarization across three case studies. Further, we use the developed optimization tool to search a virtual library of over 4M molecules for those predicted to be selective dual inhibitors of EGFR and IGF1R, acquiring 100% of the molecules that form the library’s Pareto front after exploring only 8% of the library. This workflow and associated open source software can reduce the screening burden

of molecular design projects and is complementary to research aiming to improve the accuracy of binding predictions and other molecular properties.

1 Introduction

Molecular discovery aims to identify molecules that balance multiple, often competing, properties. The need to simultaneously optimize multiple properties is especially notable in drug discovery workflows. Small molecule drugs operating through direct single-target binding interactions must exhibit not only strong binding affinity for the target protein but also minimal off-target interactions and suitable pharmacokinetic properties.¹⁻³ One formulation of small molecule drug discovery is to identify compounds that bind strongly to a protein of interest and subsequently modify them to fulfill remaining property constraints.^{1,4,5} A candidate molecule with high activity but a poor pharmacokinetic profile may ultimately be abandoned, resulting in wasted time and resources.^{3,6}

Selectivity is one property that is often considered only after a hit with promising primary activity is identified.¹ Selectivity may be measured with binding assays against off-targets that are structurally similar to the primary target or known to be associated with adverse side effects (e.g., cytochromes P450 and the hERG channel).^{3,7} Non-specific ligands that bind to many proteins in addition to the target may require additional optimization steps when compared to their selective counterparts.^{2,8} Consideration of promiscuity early in a drug discovery project may aid in deprioritizing chemical series that are inherently nonselective.^{9,10} Kinases are protein targets for which binding selectivity is particularly relevant; by screening 367 small-molecule ATP-competitive kinase inhibitors against 224 recombinant kinases, Elkins et al.¹¹ demonstrated the prevalence of unexpected cross-reactivity in identified hits: 39 of the tested compounds displayed >50% inhibition of at least 10 of the screened kinases. In other settings, binding interactions with multiple targets can be advantageous.¹² Therapeutics for Alzheimer’s disease^{13,14} and thyroid cancer^{15,16} have exhibited improved

efficacy through affinity for multiple protein targets. Optimizing affinity to multiple targets is another goal that can be brought into earlier stages of hit discovery.^{17,18}

Anticipating protein-ligand interactions that contribute to potency and selectivity is possible, albeit imperfectly, with structure-based drug design techniques that employ scoring functions to estimate energetic favorability. Docking to off-targets has been applied to improve the selectivity profiles of identified compounds.^{19–21} These demonstrations have revealed that falsely predicted non-binders may incorrectly be categorized as selective because scoring functions designed for hit-finding typically aim to minimize the false positive rate (i.e., weak binders predicted to bind strongly), not the false negative rate (i.e., binders predicted not to bind).^{21,22} Although structure-based methods like docking are limited in their predictive accuracy,^{23–28} docking-based virtual screens can still effectively enrich a virtual library for molecules that are more likely to exhibit target activity.^{29–33}

The computational cost of virtual screening³⁴ has motivated the development of model-guided optimization methods that reduce the total number of docking calculations required to recover top-performing molecules.^{35–41} As one example, Graff et al.³⁸ only require the docking scores of 2.4% of a 100M member virtual library to identify over 90% of the library’s top-50,000 ligands. Similar principles apply when using more expensive evaluations such as relative binding free energy calculations,⁴² where a reduction of computational cost can be particularly beneficial. These methods are designed to optimize a single property and are inherently *single-objective* optimizations.

The need for model-guided optimization methods in virtual screening is heightened when multiple properties are screened. The resources required for a multi-objective virtual screen scale linearly with the number of screened properties (“objectives”) and library size. In some settings, exhaustive screens of large virtual libraries (millions to billions) may be infeasible. Model-guided multi-objective optimization has the potential to reduce the computational cost of a multi-objective virtual screen without sacrificing performance. Mehta et al.⁴⁰ have previously applied multi-objective optimization with a scalarized acquisition function

to identify molecules that simultaneously optimize the docking score to Tau Tubulin Kinase 1, calculated octanol-water partition coefficient (cLogP⁴³), and synthetic accessibility score (SA_Score⁴⁴). Over 90% of the most desirable molecules were recovered after scoring of only 6% of the virtual library. Multi-objective virtual screens involve multiple design choices primarily related to the acquisition strategy, which have not yet been compared in the context of virtual screening. Further, existing methods for multi-objective virtual screening do not implement Pareto optimization. Pareto optimization aims to identify the molecules that form or are close to the *Pareto front*, for which an improvement in one objective necessitates a detriment to another. Molecules that form the Pareto front optimally balance multiple desired properties, illustrate which combinations of objective values are possible, and reveal trade-offs in the objective space; this is not possible with scalarization.

In this work, we extend the molecular pool-based active learning tool MolPAL³⁸ to this setting of multi-objective virtual screening. MolPAL is publicly available, open source, and can be adopted for multi-objective virtual screening with any desired set of objective functions, including those beyond structure-based drug design. We demonstrate through three retrospective case studies that MolPAL can efficiently search a virtual library for putative selective binders. We compare optimization performance across multi-objective acquisition functions and demonstrate the superiority of Pareto-based acquisition functions over scalarization ones. We also implement a diversity-enhanced acquisition strategy that increases the number of acquired scaffolds by 33% with only a minor impact on optimization performance. Finally, we apply MolPAL to efficiently search the Enamine Screening Collection⁴⁵ of over 4 million molecules for selective dual inhibitors of EGFR and IGF1R as an exemplary 3-objective optimization. After exploration of only 8% of the virtual library, 100% of the library’s non-dominated points and over 60% of the library’s top $\sim 0.1\%$, defined by non-dominated sorting, are identified by MolPAL.

2 Multi-Objective Virtual Screening with MolPAL

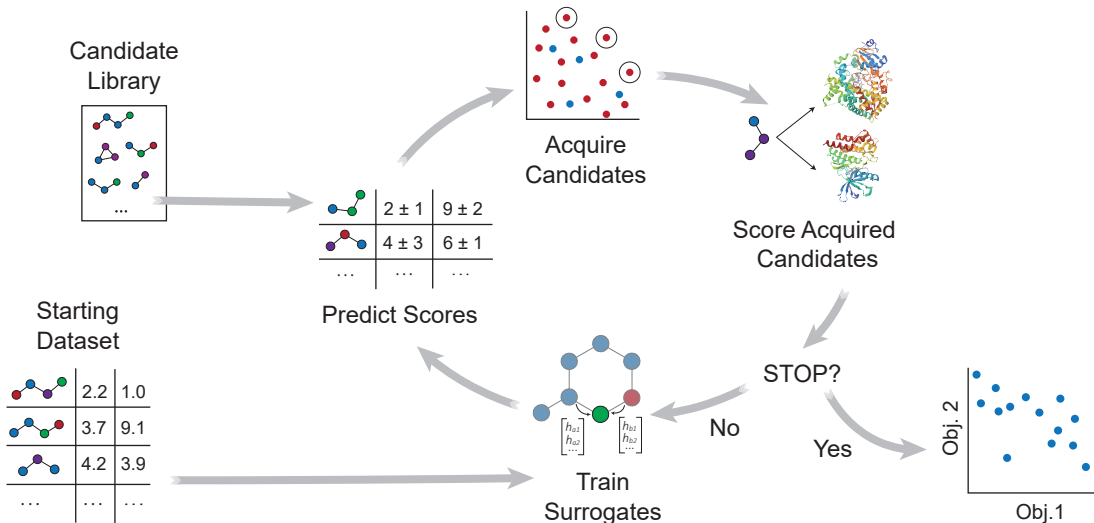


Figure 1: Overview of MolPAL’s workflow for multi-objective optimization. A surrogate model is first trained with an initial training set of randomly sampled molecules. Predictions and uncertainties from each surrogate model inform which molecules in the library to score next. After these acquired molecules are scored, each surrogate model is retrained, and the iterative loop continues. Once a stopping criterion is met, the set of observed points and their objective values can be analyzed.

MolPAL applies the multi-objective pool-based workflow described in ref. 46, combining multi-objective Bayesian optimization and surrogate models to efficiently explore a virtual library for molecules that simultaneously optimize multiple properties (Figure 1). Similar workflows have been demonstrated for the design of battery materials^{47,48} and other functional materials.^{49,50} As summarized in Algorithm S2, objective values are first calculated for a subset of the library, and surrogate models that predict each objective are trained on these initial observations. After objective values are predicted for all candidate molecules, an acquisition function selects a set of promising molecules for objective function evaluation. The surrogate models are then retrained with new observations, and the iterative loop repeats until a stopping criterion is met.

Relative to its initial release in ref. 38, MolPAL was extended primarily through modi-

fication of the acquisition strategy and handling of multiple surrogate models. The multi-objective extension of MolPAL allows users to select between Pareto optimization and scalarization strategies.

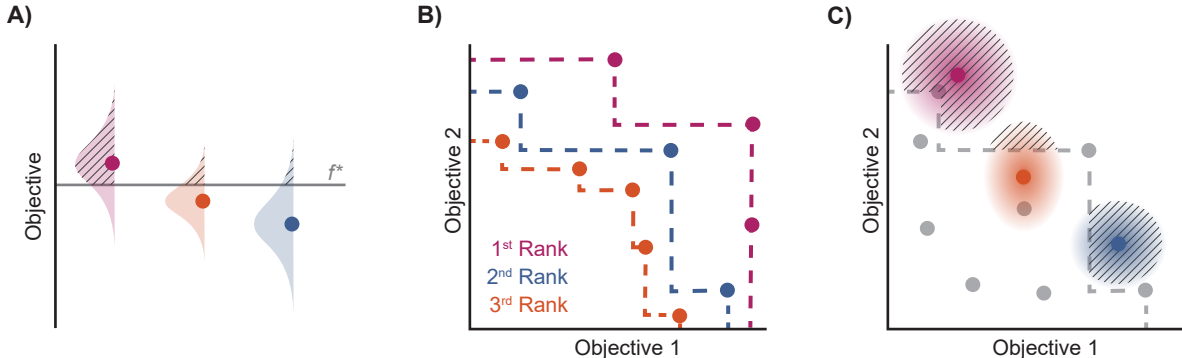


Figure 2: Depiction of acquisition functions in Bayesian optimization. (A) Probability of improvement (PI) estimates the likelihood that an as-yet unobserved objective function value exceeds the current maximum value f^* . Expected improvement (EI) estimates the amount that f^* would increase if an unobserved point is acquired.⁵¹ (B) Non-dominated sorting assigns integer ‘‘Pareto ranks’’ to each candidate. (C) Hypervolume-based acquisition functions⁵¹ extend the principles of PI and EI to multiple dimensions using the observed Pareto front (grey dashed line) rather than f^* . Probability of hypervolume improvement (PHI) represents the likelihood that acquisition of an unobserved point would increase the hypervolume by any amount. Expected hypervolume improvement (EHI) estimates the increase in hypervolume if the objective function value of such a point is scored.⁵¹ Objectives are defined so that optimization corresponds to maximization.

Scalarization reduces a multi-objective optimization problem into a single-objective problem, often through a weighted sum:

$$f_{scal}(x) = \sum_i \lambda_i f_i(x), \quad (1)$$

with each λ_i denoting the relative importance of objective f_i . Weighted sum scalarization requires the relative importance of objectives to be known before the optimization in order to assign weighting factors λ . Alternative scalarization strategies beyond a weighted sum include random scalarization^{52,53} and Chebyshev scalarization,^{54,55} but these are not yet implemented in MolPAL. Scalarization enables the use of single-objective acquisition functions, which include probability of improvement (PI)⁵⁶ or expected improvement (EI)⁵⁷

(Figure 2A), greedy, and upper confidence bound (UCB)⁵⁸ (Table 1). Scalarization is implemented prior to surrogate model training, i.e., only one single-task surrogate model is necessary. Algorithm S1 summarizes MolPAL’s implementation of scalarized multi-objective optimization.

Pareto optimization is a multi-objective optimization strategy that reveals the trade-offs between objectives and does not require any measure of the relative importance of objectives. Further, Pareto optimization aims to identify the entire Pareto front, a feature not guaranteed by single-objective methods such as weighted sum scalarization.^{59,60} Common multi-objective acquisition functions include the probability of hypervolume improvement (PHI),⁵¹ expected hypervolume improvement (EHI),⁵¹ non-dominated sorting (NDS),^{61,62} and Pareto upper confidence bound (P-UCB).⁶³ These are natural extensions of single-objective acquisition functions (Table 1) that instead aim to increase the region, or *hypervolume*, dominated by the acquired points (Figure 2). P-UCB and its single-objective analog UCB are not considered in this work. For model-guided Pareto optimization, either a multi-task surrogate model, multiple single-task surrogate models, or a combination thereof is needed to predict the set of objective function values. As outlined in Algorithm S2, MolPAL trains N single-task surrogate models to predict N objectives to circumvent the challenge of loss function weighting in multi-task learning.⁶⁴

Table 1: Common single-objective acquisition functions and their multi-objective analogs. \mathbb{P} and \mathbb{E} represent probability and expected value, respectively. f^* is the current best objective value, HV is hypervolume, and $\mathbf{rank}()$ is the Pareto rank. Surrogate models provide prediction means μ and standard deviations σ for the objective value f of candidate point x . \mathcal{X}_{acq} is the set of points acquired in previous iterations. Bold variables are vectors. $\mathcal{N}(\boldsymbol{\mu}, \boldsymbol{\sigma})$ implies that the covariance matrix is treated as diagonal with entries σ_i^2 , i.e., uncertainty is uncorrelated across objective functions.

Single-objective		Multi-objective	
PI ⁵⁶	$\mathbb{P}_{f(x) \sim \mathcal{N}(\mu(x), \sigma(x))} [f(x) > f^*]$	PHI ⁵¹	$\mathbb{P}_{\mathbf{f}(x) \sim \mathcal{N}(\boldsymbol{\mu}(x), \boldsymbol{\sigma}(x))} [\text{HV}(\mathcal{X}_{acq} \cup x) > \text{HV}(\mathcal{X}_{acq})]$
EI ⁵⁷	$\mathbb{E}_{f(x) \sim \mathcal{N}(\mu(x), \sigma(x))} [\max\{f(x) - f^*, 0\}]$	EHI ⁵¹	$\mathbb{E}_{\mathbf{f}(x) \sim \mathcal{N}(\boldsymbol{\mu}(x), \boldsymbol{\sigma}(x))} [\text{HV}(\mathcal{X}_{acq} \cup x) - \text{HV}(\mathcal{X}_{acq})]$
Greedy	$\mu(x)$	NDS ^{61,62}	$\mathbf{rank}(\boldsymbol{\mu}(x))$
UCB ⁵⁸	$\mu(x) + \beta\sigma(x)$	P-UCB ⁶³	$\mathbf{rank}(\boldsymbol{\mu}(x) + \beta\boldsymbol{\sigma}(x))$

Acquiring a batch of k points in a single iteration may be more efficient than sequential acquisition when objectives functions can be calculated in parallel. "Top- k batching" naively selects the k points with the highest acquisition scores.⁶⁵ More sophisticated batch acquisition strategies iteratively construct optimal batches one point at a time by hallucinating objective function values.⁶⁶⁻⁷¹ Other strategies use heuristics to select batches that are diverse in the design space or objective space in order to improve the utility of a batch.⁷²⁻⁷⁷ MolPAL implements both naive top- k batching and diversity-enhanced acquisition strategies that apply clustering in both the design space and in the objective space (Section 5.5).

3 Results and Discussion

3.1 Description of Case Studies

We test MolPAL with three retrospective case studies with an emphasis on docking-predicted binding selectivity to compare optimization performance across acquisition functions. The pairs of objectives used in these case studies are exclusively docking scores even though the framework of MolPAL is more general. Each case explores a virtual library of approximately 260k molecules and optimizes two competing docking score objectives from the DOCK-STRING benchmark.⁷⁸ Case 1’s goal is modeled after identifying antagonists of dopamine receptor D₃ (DRD3) that are selective over dopamine receptor D₂ (DRD2), which may enable effective treatment of various conditions without the side effects triggered by DRD2 antagonists.⁷⁹⁻⁸¹ Case 2 treats Janus Kinase 2 (JAK2), a leukemia target, as the on-target and lymphocyte-specific protein tyrosine kinase (LCK) as the off-target.^{82,83} Finally, Case 3 aims to identify selective inhibitors of insulin-like growth factor 1 receptor (IGF1R)^{84,85} that do not bind to cytochrome P450 3A4 (CYP3A4),^{86,87} an off-target known to impact the pharmacokinetic properties of drugs through metabolism.⁸⁸⁻⁹⁰ The property trade-offs for each case are shown in Figure 3. Because both positive docking scores and scores of 0 should be interpreted as non-binders, we clip docking scores to 0.

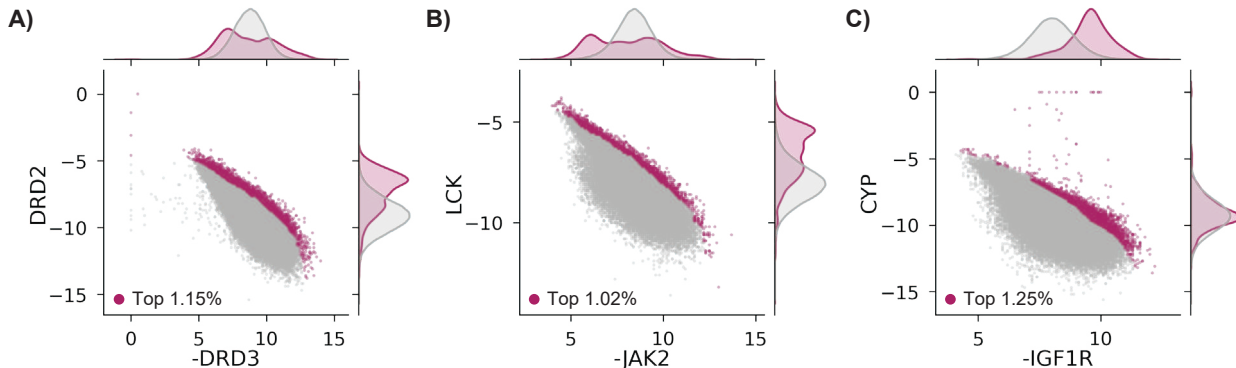


Figure 3: Docking scores in the DOCKSTRING dataset⁷⁸ for (A) Case 1, (B) Case 2, and (C) Case 3. All molecules considered in the top $\sim 1\%$, as determined by NDS rank (Section 5.6), are shown as magenta points, with the remaining data in grey. There are 2986 (1.15%), 2651 (1.02%), and 3261 (1.25%) molecules in the top $\sim 1\%$ for Cases 1, 2, and 3, respectively.

We employ single-task directed message-passing neural networks^{91,92} for each objective as surrogate models (Section 5.4). An initial set of 2,602 molecules is randomly sampled at the zeroth iteration, and 1% of the library (2,602 molecules) is acquired in each subsequent iteration. Scalarization weighting factors (λ_1 and λ_2 in Eq. 1) were set to 0.5. Five trials with distinct initialization seeds were completed for each acquisition function. Section 5 contains full implementation details.

3.2 Pareto Acquisition Functions Outperform Scalarization

We characterize optimization performance with four metrics: fraction of the top $\sim 1\%$ acquired, inverted generational distance (IGD), hypervolume (HV), and fraction of non-dominated points acquired. We motivate the selection of these metrics and describe their implementation in Section 5.6.

All Pareto optimization acquisition functions show substantial improvement over random acquisition according to the top $\sim 1\%$ metric, with PHI performing most consistently across cases (Figure 4A-F). Analyzing the same metric, greedy is clearly the best scalarized acquisition function despite its poor performance in Case 3 relative to PHI and EHI. Only in Case 1 does the best scalarization acquisition function outperform the best Pareto acquisition

function.

There is better differentiation among acquisition functions in terms of the IGD (Figure 4G-I). EHI achieves the smallest IGD in Cases 1 and 3, while all three Pareto acquisition functions perform similarly in Case 2. When performance is measured by the fraction of non-dominated points acquired, EHI and PHI outperform scalarization acquisition functions (Figure 5) even though the degree of improvement varies across cases. The sensitivity of the hypervolume metric to outliers on the Pareto front leads to noisy hypervolume profiles that follow the same trends as the IGD metric (Figure S2). Overall, Pareto optimization acquisition functions strongly outperform or match the performance of scalarization for the pairs of objectives and virtual library considered.

The variation in relative performance of different acquisition functions across evaluation metrics is noteworthy. For example, greedy scalarization performs quite well in the top $\sim 1\%$ metric for all cases but worse than random acquisition according to IGD, hypervolume, and fraction of non-dominated points in Case 3. The results shown here highlight the importance of assessing the performance across different sets of objectives. Despite the variation across cases and metrics, EHI and PHI consistently perform as well as scalarization or substantially better than scalarization. These acquisition functions are suitable choices for new sets of objectives. Alternatively, when a previously unexplored set of objectives is to be optimized, a retrospective study on a scored subset of the library can inform the selection of a suitable acquisition strategy. Each reported metric corresponds to distinct optimization goals (Section 5.6); the primary application of a multi-objective virtual screen should inform which metric to use for acquisition function comparison and selection.

3.3 Clustering-based Acquisition Improves Molecular Diversity

Scoring functions used in structure-based virtual screening can exhibit systematic errors that bias selection toward specific interactions.⁹³ This poses a risk for experimental validation if specific scaffolds are overrepresented in the top-scoring molecules. Selecting a structurally

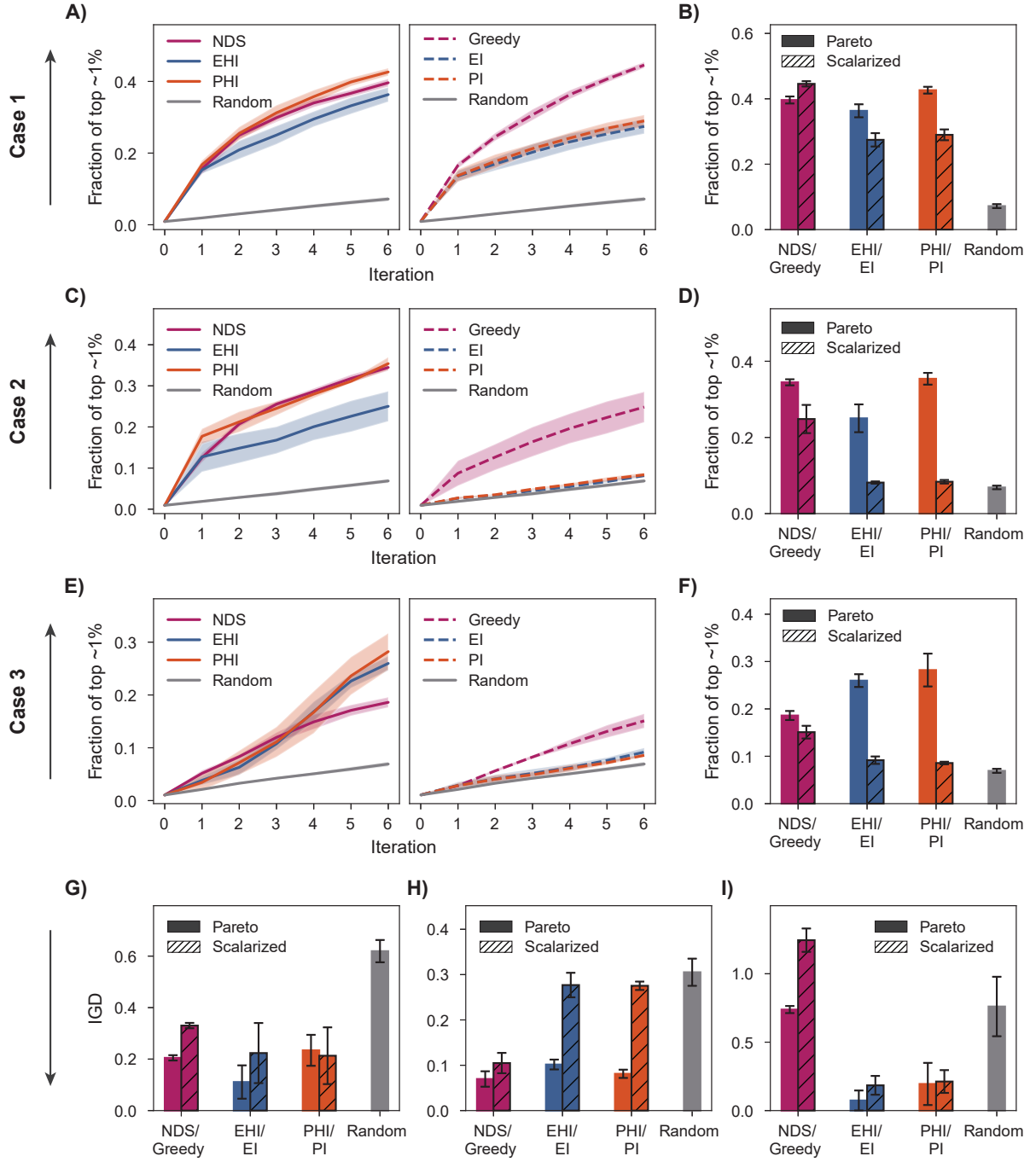


Figure 4: Fraction of the top $\sim 1\%$ acquired and inverted generational distance (IGD) for Case 1, 2, and 3. (A, C, E) Fraction of top $\sim 1\%$ using Pareto optimization acquisition functions (left) and scalarized acquisition functions (right). (B, D, F) Fraction of the top $\sim 1\%$ acquired after 6 iterations. (G-I) IGD after 6 iterations for Case 1 (G), Case 2 (H), and Case 3 (I). Error bars (B, D, F, G-I) and shaded regions (A, C, E) denote ± 1 standard deviation across five runs.

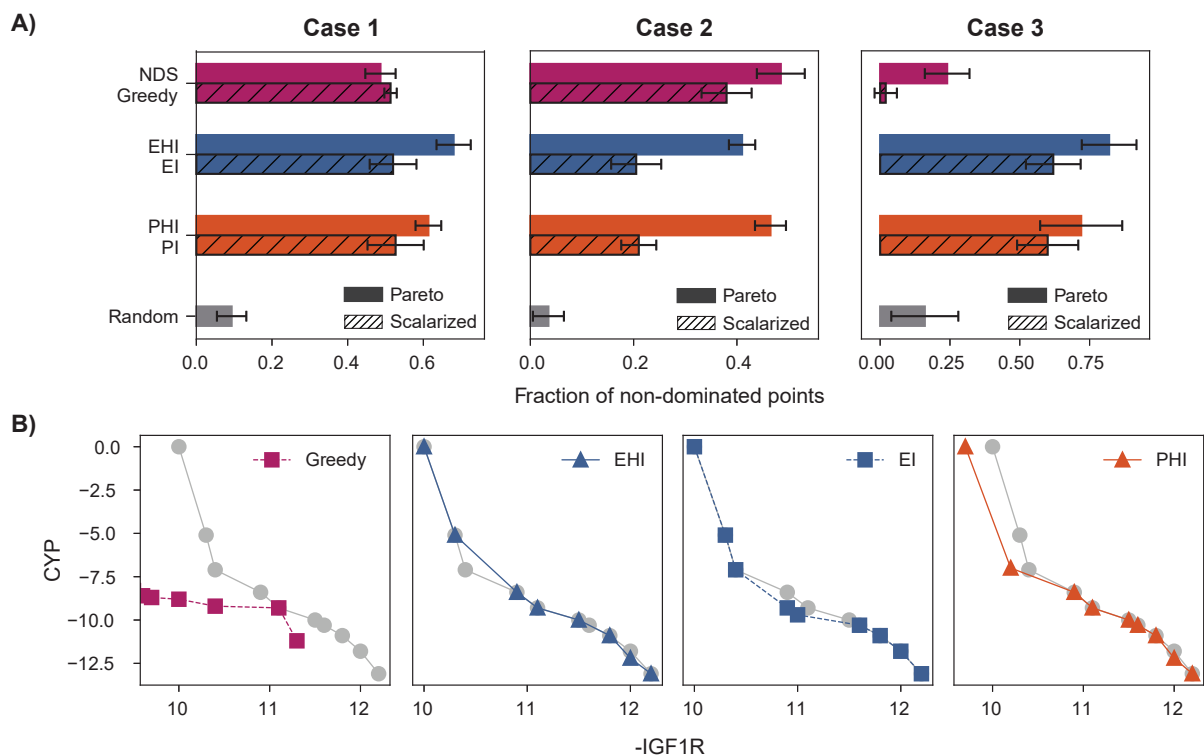


Figure 5: Identification of molecules on the true Pareto front. **(A)** Fraction of non-dominated points acquired for Cases 1, 2, and 3. **(B)** Final Pareto front acquired in Case 3 using probability of greedy, expected hypervolume improvement (EHI), expected improvement (EI), and hypervolume improvement (PHI) acquisition, with the true Pareto front shown in grey. The Pareto front identified with greedy acquisition poorly reflects the shape of the true Pareto front, a discrepancy captured well by the fraction of non-dominated points metric. Each plot represents individual runs, all initialized with the same model seed and starting acquired set. Error bars denote \pm one standard deviation across five runs.

diverse set of candidates is one strategy to mitigate this risk and can be achieved via a diversity-enhanced acquisition strategy (Section 5.5). First, a set of molecules larger than the target batch size is selected according to the acquisition function and is then partitioned into a number of clusters equal to the batch size in feature (e.g., molecular fingerprint) space. The molecule with the best acquisition score in each cluster is acquired. We analyzed the performance of diversity-enhanced acquisition for Case 3, using PHI as the acquisition function. All hyperparameters were the same as those used for previous experiments (Section 5).

Feature space clustering slightly hinders optimization performance according to all four performance metrics (Figure 6A-E), but it also increases the number of graph-based Bemis-Murcko scaffolds⁹⁴ acquired by 33% when compared to a naïve batch construction strategy. This degradation in measured performance is expected given that the performance metrics do not consider the overall diversity of the selected molecules. The increased structural diversity of the selected molecules can be qualitatively visualized via dimensionality reduction through UMAP⁹⁵ (Figure S3).

Certain multi-objective optimization methods such as NSGA-II⁶² also incorporate *objective space* diversity, i.e., the selection of points better distributed along the Pareto front.⁴⁶ We find that clustering in the objective space during acquisition (Section 5.5) mildly hinders performance in all optimization metrics (Figure 6A-E). An acquisition strategy that considers diversity in both the objective space and feature space (Section 5.5) performs similarly to the standard acquisition strategy across most optimization metrics (Figure 6A-D) while acquiring a more structurally diverse set of molecules when compared to standard acquisition (Figure 6F and S3). Overall, we recommend the use of feature space clustering if having structurally distinct candidates is a priority for experimental validation.

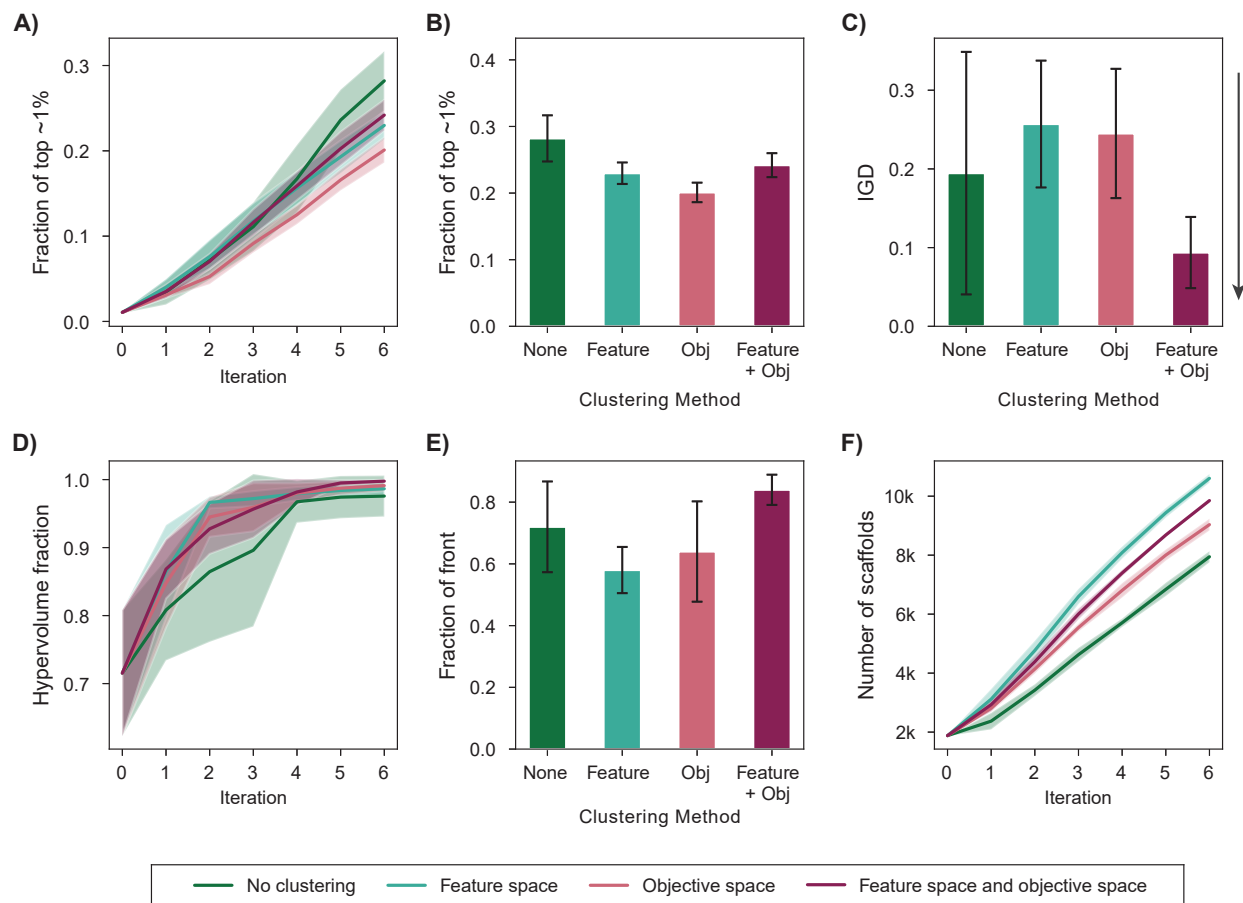


Figure 6: Impact of clustering in fingerprint and objective space on optimization performance. **(A)** Fraction of top ~1% acquired. **(B)** Fraction of top ~1% acquired after 6 iterations. **(C)** Inverted generational distance (IGD) after 6 iterations. **(D)** Hypervolume profiles. **(E)** Fraction of the library's non-dominated points acquired after 6 iterations. **(F)** Number of distinct graph-based Bemis-Murcko scaffolds acquired. Error bars (B, C, E) and shaded regions (A, D, F) denote \pm one standard deviation across five runs.

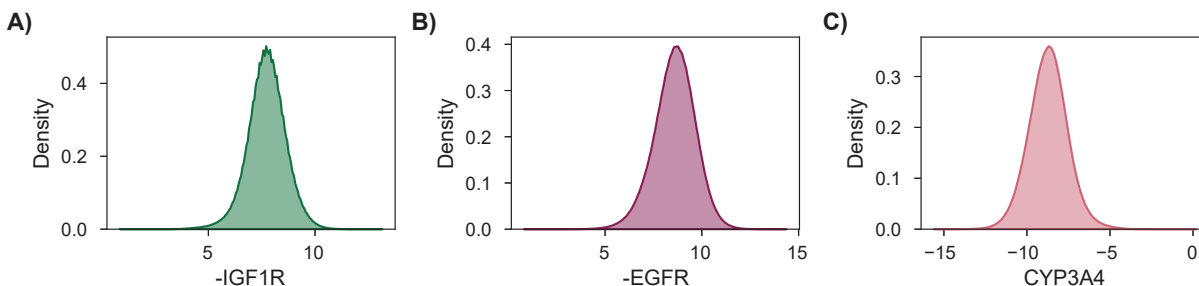


Figure 7: Distributions of objective function values to be maximized for a retrospective 3-objective virtual screen. **(A,B)** Docking scores for targets IGF1R and EGFR, respectively. **(C)** Docking scores for off-target CYP3A4.

3.4 MolPAL Scales to 3 Objectives and Larger Libraries

As a final demonstration, we show that MolPAL scales well to larger virtual libraries and more than two objectives by searching the Enamine Screening Library⁴⁵ of over 4 million molecules for those that optimize three docking objectives. The objectives were defined to identify putative dual inhibitors of IGF1R and EGFR^{96–98} with selectivity over CYP3A4,^{88–90,99} which could in principle serve as starting points for esophageal cancer therapeutics. To analyze performance according to the four considered evaluation metrics, we perform this search retrospectively after docking the entire library using DOCKSTRING’s protocol for each target⁷⁸ (Section 5.1). The distributions of individual objectives for the entire library are shown in Figure 7. We use PHI acquisition without clustering and acquire 1% of the library at each iteration, repeating each experiment three times.

Table 2: Performance metrics after acquisition of 10% of the library. Means and standard deviation across three trials are shown. Metrics include hypervolume (HV) and inverted generational distance (IGD), as well as the fraction of the library’s top 0.12% (4829 molecules), top 0.524% (21015 molecules), and Pareto front points (39 molecules) acquired.

Acquisition Function	Top $\sim 0.1\%$ \uparrow	Top $\sim 0.5\%$ \uparrow	HV \uparrow	IGD \downarrow	Fraction of True Front \uparrow
PHI	0.65 ± 0.06	0.50 ± 0.09	1.00 ± 0.00	0.00 ± 0.00	1.00 ± 0.00
Random	0.10 ± 0.00	0.10 ± 0.00	0.81 ± 0.05	0.88 ± 0.04	0.10 ± 0.04

MolPAL succeeds in acquiring 100% of the library’s non-dominated points in all three replicates after exploring only 8% of the search space (Figure 8C), a 9X improvement of in the fraction of acquired non-dominated points over random acquisition. At this same degree of exploration (8% of the library), over 60% of the library’s top $\sim 0.1\%$ molecules have been identified (Figure 8A). Improvements in IGD and hypervolume with MolPAL over random acquisition are also notable (Figure 8, Table 2). The results of this retrospective run indicate that MolPAL can substantially reduce the computational resources required to identify molecules that simultaneously optimize multiple properties from a virtual library of millions of molecules.

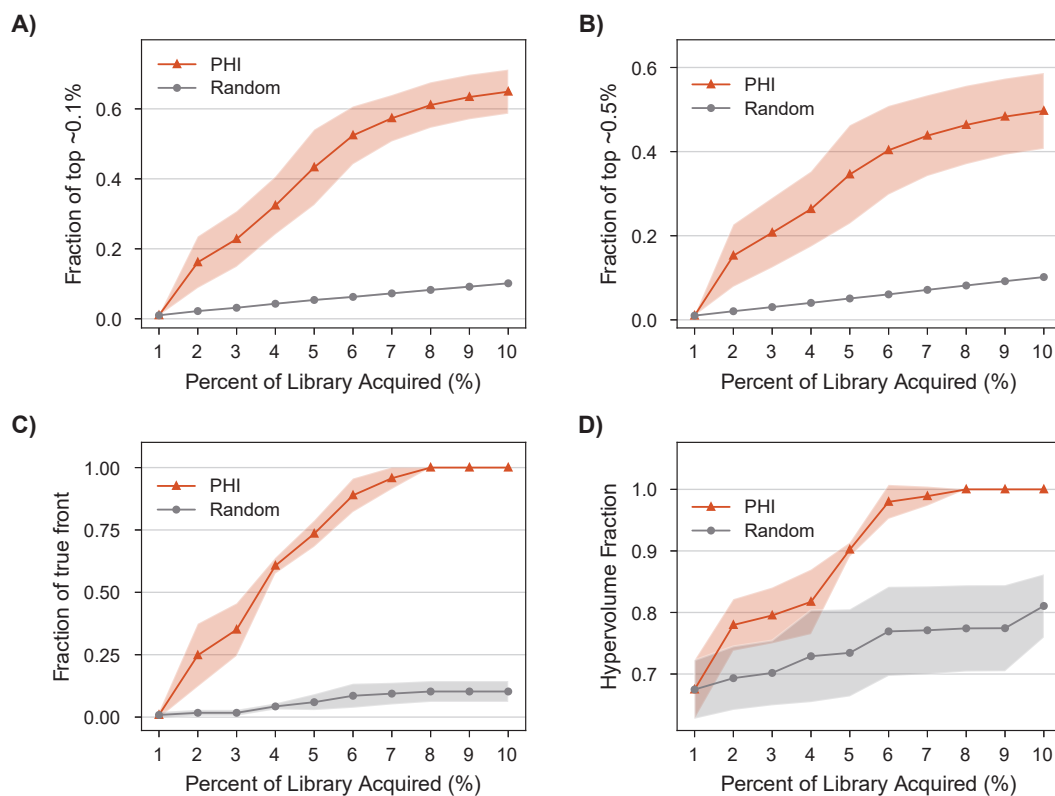


Figure 8: Performance of MolPAL for the identification of selective dual IGF1R/EGFR inhibitors from the 4M-member Enamine screening library as an exemplary three-objective optimization. Profiles are depicted for the fraction of (A) top $\sim 0.1\%$, (B) top $\sim 0.5\%$, and (C) non-dominated points acquired, as well as the (D) hypervolume.

The virtual library’s true Pareto front of 39 molecules, all of which were recovered by MolPAL, is visualized in Figure 9. The structures of all non-dominated molecules are shown in Figures S5-S7. The structures of these molecules expose some remaining challenges of docking for selectivity prediction. Molecules predicted to be non-binders to CYP3A4, such as M2 and M20 in Figure 9, are relatively large molecules that do not fit inside the pocket of CYP3A4, leading to steric clashes and less favorable binding energetics. The ability for such molecules to score well against the IGF1R and EGFR but poorly against CYP3A4 is exemplified by the computed docking poses and protein-ligand interactions of M2 (Figure S4). Although steric clashes may be a valid reason for hypothetical selectivity towards EGFR/IGF1R over CYP3A4, the molecules predicted to be most selective (e.g., M2 and M20) are not attractive candidates for experimental validation. In practice, dominated molecules that are close to the identified Pareto front should also be considered for experimental validation or follow-up studies. A ligand efficiency score may also be used as an objective function to penalize very large molecules.¹⁰⁰ Nevertheless, given the imperfections of docking as an oracle function, MolPAL perfectly identifies the Pareto front at a reduced computational cost and scores well in terms of all evaluation metrics. We do not intend to nominate the visualized molecules as starting points for a drug discovery project but instead aim to demonstrate the ability for MolPAL to efficiently identify molecules that optimize any set of oracles such as those that predict binding affinity.

4 Conclusion

We have introduced an open source multi-objective extension of the pool-based optimization tool MolPAL³⁸ and demonstrated its ability to accelerate multi-objective virtual screening. MolPAL provides a flexible Pareto optimization framework that allows users to systematically vary key design choices like acquisition strategy. MolPAL is most appropriate for optimizing objectives that are more expensive to calculate than surrogate molecular prop-

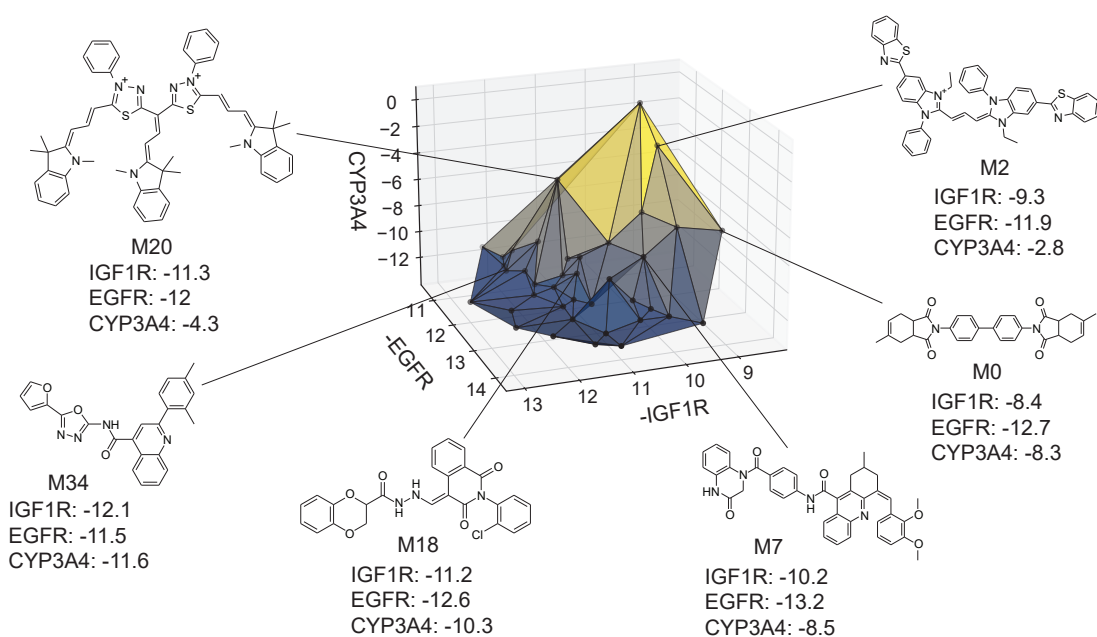


Figure 9: Visualization of the Pareto front for the 3-objective optimization for the identification of putative selective dual inhibitors. All non-dominated points depicted were acquired by MolPAL after scoring only 8% of the virtual library. Structures for some molecules on the Pareto front are shown. Docking scores to targets EGFR and IGF1R and off-target CYP3A4 were calculated with the AutoDock Vina wrapper DOCKSTRING.⁷⁸

erty prediction models. Beyond docking, these include objectives that require binding free energy calculations, quantum mechanical simulations, or experiments to measure. Objectives that are calculable in CPU milliseconds, such as SA_Score or ClogP, can be screened exhaustively and do not warrant model-guided optimization tools. MolPAL could also be applied to consensus docking by optimizing multiple scoring functions that predict binding affinity to the same target.¹⁰¹

We first assessed MolPAL on three two-objective case studies that aim to identify putative selective binders. We found that expected hypervolume improvement and probability of hypervolume improvement, both Pareto optimization acquisition functions, consistently performed as well as or better than scalarization. A diversity-enhanced acquisition strategy that applies clustering in molecular fingerprint space was found to increase the number of Bemis-Murcko scaffolds observed by 33% when compared to standard acquisition. Finally, we demonstrated that MolPAL can efficiently search large virtual libraries and optimize three objectives simultaneously through a case study aiming to identify putative selective dual inhibitors from the Enamine Screening Library of over 4 million molecules; MolPAL acquired all of the library’s non-dominated molecules after exploring only 8% of the library in all three replicates.

Exploration of other multi-objective optimization approaches, such as random scalarization and Chebyshev scalarization, in the context of molecular optimization could expose benefits of strategies not explored in this work. Other published diversity-enhanced acquisition strategies^{77,102} may have the potential to improve both molecular diversity *and* optimization performance.

While the use of docking to off-targets as a proxy for selectivity is well precedented,^{19–21} the high false negative rates of docking screens (i.e., binders predicted to be nonbinding) pose a risk for experimental validation of molecules predicted to be selective.^{21,22,103} Pharmacophore models and scoring functions that are designed for off-target activity^{9,20,104} could be more appropriate for cross-docking for selectivity in the future. Because MolPAL is a

general multi-objective optimization strategy that can be applied to any combination of oracle functions, it will maintain its relevance as these oracle functions improve in time. Future efforts applying MolPAL to hit discovery and early-stage molecular design are necessary to validate the benefits of considering multiple objectives at early stages of molecular discovery.

5 Methods

All code required to reproduce the reported results can be found in the `multiobj` branch of MolPAL at <https://github.com/coleygroup/molpal/tree/multiobj>.

5.1 Data Collection

All docking scores used in Sections 3.2 and 3.3 were used without reprocessing from the DOCKSTRING benchmark.⁷⁸ For the larger scale study in Section 3.4, the Enamine Screening library of over 4 million compounds⁴⁵ was docked against IGF1R, EGFR, and CYP3A4 using DOCKSTRING⁷⁸ with default settings for each target. Before docking, molecules were stripped of salts using RDKit’s SaltRemover module.¹⁰⁵ Of the 4,032,152 in the library (at the time of download), 4,010,199 were docked successfully to CYP3A4, 4,010,191 to IGF1R, and 4,010,187 to EGFR. The full set of docking scores are available at https://figshare.com/articles/dataset/Enamine_screen_CYP3A4_EGFR_IGF1R_zip/23978547.

5.2 Objectives

Docking scores to on-targets were minimized objectives, and scores to off-targets were maximized objectives. A positive docking score is not meaningfully different from a docking score of zero. We therefore adjust docking objectives to be:

$$f_{dock}(x) = \min(0, f(x)) \tag{2}$$

where $f(x)$ is the raw docking score and $f_{\text{dock}}(x)$ is the minimized (for on-targets) or maximized (for off-targets) objective. Clipping docking scores in this manner also mitigates the effect of outliers on Pareto optimization metrics like hypervolume.

5.3 Acquisition Functions

We modify PHYSBO’s implementation¹⁰⁶ of expected hypervolume improvement and probability of hypervolume improvement, which applies the algorithm proposed by Couckuyt et al.¹⁰⁷. MolPAL uses the `non_dominated_front_2d()` utility in `pygmo`¹⁰⁸ for non-dominated sorting in two dimensions. In more than three dimensions, MolPAL iteratively identifies non-dominated points using the Pareto class in PHYSBO¹⁰⁶ and removes those points from the unranked set until enough points have been ranked.

In the scalarization runs, f was calculated according to Eq. 1 with $\lambda_1 = \lambda_2 = 0.5$. For prediction mean μ , prediction standard deviation σ , and current maximum value f^* , expected improvement and probability of improvement in the scalarization runs were calculated as:

$$\begin{aligned} \text{EI}(x, f^*) &= (\mu(x) - f^* + \xi) \cdot \Phi\left(\frac{\mu(x) - f^* + \xi}{\sigma(x)}\right) + \sigma(x) \cdot \phi\left(\frac{\mu(x) - f^* + \xi}{\sigma(x)}\right) \\ \text{PI}(x, f^*) &= \Phi\left(\frac{\mu(x) - f^* + \xi}{\sigma(x)}\right) \\ \text{Greedy}(x) &= \mu(x) \end{aligned} \tag{3}$$

where Φ is the cumulative distribution function of the standard normal distribution and ϕ is the probability density function of the standard normal distribution function. ξ is a hyperparameter that controls the competitiveness of the sampling,⁵⁶ which we set to 0.01. Higher values of ξ encourages exploration of uncertain points, while low values prioritize prediction means.⁵⁶

5.4 Surrogate Model

Because the optimization campaigns explored in this study comprise batches of thousands of molecules, we elect to use a directed message-passing neural network architecture⁹¹ as the surrogate model for all runs. MolPAL contains a PyTorch¹⁰⁹ implementation of ChemProp^{91,92} as in the original publication.³⁸ We use an encoder depth of 3, directed edge messages only (no atom messages), a hidden size of 300, ReLU activation, and two layers in the feed-forward neural network as default parameters. The model was trained with an initial learning rate of 10^{-4} using a Noam learning rate scheduler and an Adam optimizer. In each iteration, the model is retrained from scratch, as this was found to provide a benefit over fine-tuning.³⁸

We use mean-variance estimation^{110,111} for surrogate model uncertainty quantification. The surrogate model is trained to predict both the mean $f(x)$ and the variance of the estimation $\sigma^2(x)$ via a negative log likelihood loss function:

$$L(f(x), \mu(x), \sigma(x)) = \frac{\ln 2\pi}{2} + \frac{1}{2} \ln \sigma^2(x) + \frac{(\mu(x) - y(x))^2}{2\sigma^2(x)} \quad (4)$$

where $f(x)$ is the true objective value, μ is the predicted mean, and $\sigma^2(x)$ is the predicted variance.

5.5 Clustering

We implement three diversity-enhancing acquisition strategies using clustering: in the feature space, in the objective space, and in both (Section 3.3). Feature space clustering is performed according to 2048-bit atom-pair fingerprints¹¹² calculated using the `GetHashedAtomPairFingerprintAsBitVect` function in RDKit¹⁰⁵ with the minimum length and maximum length of paths between pairs to 1 and 3, respectively. Atom pair fingerprints have been shown to outperform other extended connectivity fingerprints in recovering 3D-shape analogs¹¹³ and ranking close analogs by structural similarity.¹¹⁴ The predicted objective means were used for clustering in the objective space.

The acquisition strategy first selects a superset of molecules according to the acquisition scores as in a standard acquisition strategy. In our trials, the size of the superset is 10X the batch size, b . Then, the superset is clustered according to molecular fingerprints or predicted objective values. We use the implementation of `MiniBatchKMeans`¹¹⁵ in `scikit-learn`¹¹⁶ with b clusters, 10 random initializations, an initialization size of $3b$, and a reassignment ratio of 0 for batch size b . Although b clusters are specified, some clusters may be returned as empty in the case of a low-dimensional cluster basis. We ensure that b points are acquired by iteratively looping through all clusters, beginning with the largest clusters, and acquiring the molecule in the cluster with the highest acquisition score. This process is continued until b molecules are acquired.

When clustering in *both* the feature and objective spaces, the superset is first clustered in the objective space into $\text{ceil}(b/2)$ clusters, and $\text{ceil}(b/2)$ points are acquired by iterating through the clusters and selecting the molecule with the highest acquisition score. The superset is then supplemented with the $b/2$ unacquired candidate points that have the highest acquisition scores. Then, the superset is clustered in the atom-pair fingerprint space into $b - \text{ceil}(b/2)$ clusters, and the point with the highest acquisition score in each cluster is acquired. Thus, when both forms of clustering are used, effectively $b/2$ points are selected to improve objective space diversity, and $b/2$ points are selected to improve feature space diversity.

5.6 Performance Metrics

Four performance metrics designed for Pareto optimization were measured to holistically assess the performance of MolPAL. The underlying goal of a multi-property virtual screen (e.g., understanding the trade-offs between objectives, identifying a set of potentially promising selective inhibitors) can guide which evaluation metric to be deemed most important. Reported metrics and the motivation for selecting each is described below.

Fraction of top $\sim k\%$

Virtual screening workflows based on active learning are often evaluated using a top- k metric: the fraction of the true top- k molecules that have been acquired. Using a top- k metric captures the goal of separating promising molecules from the bulk while acknowledging that docking scores are imperfect and imprecise predictors of binding affinity. The best observed performance of a single compound is a less useful metric in this context, as there is a high likelihood it would not validate as a binder experimentally.

For multi-property virtual screening, the set of top- k molecules is not well-defined. We opt to define the top $\sim k\%$ through non-dominated sorting of the library (Figure S1). The non-dominated points in the library are iteratively selected and removed from the candidate pool until $\geq k\%$ of the library has been selected. These points then serve as the top $\sim k\%$. Because multiple points are selected as part of the top $\sim k\%$ in each iteration (i.e., all points of a certain Pareto rank), the fraction is slightly larger than $k\%$.

The top $\sim k\%$ metric best describes virtual screens aiming to identify many molecules roughly close to the Pareto front. Compared to other metrics that consider points on or much closer to the Pareto front, it best captures the expectation that not all top-performing molecules will validate experimentally.

Fraction of non-dominated points

In some multi-property screens, the aim may be to elucidate as many points on the true Pareto front as possible. This enables the shape of the Pareto front and the inherent trade-off between objectives to be well-understood. A metric related to only the true non-dominated points is most appropriate in these cases. The library’s non-dominated points are identified using non-dominated sorting (Section 5.3), and this metric is simply the fraction of the non-dominated molecules that were acquired.

Hypervolume

Hypervolume is a common metric used to assess the performance of multi-objective optimization methods.¹¹⁷ It measures the size of the region dominated by the Pareto front; in a bi-objective optimization, the hypervolume is the area dominated by the acquired points (Figure S1B). Importantly, the hypervolume can be very sensitive to outliers, leading to high variability across repeat experiments. Because outliers may fail to be experimentally validated, the strong sensitivity of hypervolume to specific points makes it slightly misleading. We use the python package `pygmo`¹⁰⁸ to calculate hypervolume and report it as the fraction of the virtual library’s total hypervolume. In contrast to the other evaluated metrics, the absolute hypervolume can be measured in prospective studies.

Inverted generational distance

The inverted generational distance (IGD), another widely adopted metric for Pareto optimization performance,^{117,118} quantifies the distance between the true Pareto front and the Pareto front of the acquired points. Therefore, IGD is a useful metric for understanding the extent to which the shape of the true Pareto front is captured by the acquired points. The IGD is computed as the average of the shortest distance between each point on the true Pareto front and the set of acquired points (Figure S1):

$$\text{IGD}(\mathcal{X}_{acq}, Z) = \frac{1}{|Z|} \sum_{z \in Z} \min_{x \in \mathcal{X}_{acq}} d(x, z), \quad (5)$$

where \mathcal{X}_{acq} is the set of acquired points, Z is the set of non-dominated points, and $d(x, z)$ is the Euclidian distance between acquired point x and non-dominated point z in the objective space. IGD is calculated with the python package `pymoo`.¹¹⁹

5.7 Scaffold Analysis

To quantify the improvement in molecular diversity using diversity-enhanced acquisition, we count the number of observed Bemis-Murcko scaffolds⁹⁴ using RDKit’s `MurckoScaffoldSmilesFromSmiles` and `MakeScaffoldGeneric` functions.

Data Availability

All code required to reproduce the reported results can be found in the `multiobj` branch of MolPAL at <https://github.com/coleygroup/molpal/tree/multiobj>. Docking scores from the DOCKSTRING benchmark are available at https://figshare.com/articles/dataset/dockstring_dataset/16511577. Docking scores for IGF1R, EGFR, and CYP3A4 computed as a part of this work can be found at https://figshare.com/articles/dataset/Enamine_screen_CYP3A4_EGFR_IGF1R_zip/23978547.

Author Contributions

J. C. F. extended MolPAL to perform multi-objective optimization and conducted the experiments; J. C. F., D. E. G., and C. W. C. designed the experiments; J. C. F., D. E. G., and C. W. C. wrote the manuscript. C. W. C. supervised the work.

Conflicts of Interest

There are no conflicts to declare.

Acknowledgment

This work was funded by the DARPA Accelerated Molecular Discovery program under contract number HR00111920025. J.C.F. received additional support from the National Science

Foundation Graduate Research Fellowship under Grant No. 2141064. The authors acknowledge the MIT SuperCloud,¹²⁰ Lincoln Laboratory Supercomputing Center, and the MIT Engaging Cluster for providing HPC resources that have contributed to the research results reported within this paper. The authors thank Samuel Goldman for helpful discussions about the content of this manuscript.

References

- (1) Hughes, J.; Rees, S.; Kalindjian, S.; Philpott, K. Principles of Early Drug Discovery. *British Journal of Pharmacology* **2011**, *162*, 1239–1249.
- (2) Kettle, J. G.; Wilson, D. M. Standing on the Shoulders of Giants: A Retrospective Analysis of Kinase Drug Discovery at Astrazeneca. *Drug Discovery Today* **2016**, *21*, 1596–1608.
- (3) Beckers, M.; Fechner, N.; Stiefl, N. 25 Years of Small-Molecule Optimization at Novartis: A Retrospective Analysis of Chemical Series Evolution. *Journal of Chemical Information and Modeling* **2022**, *62*, 6002–6021.
- (4) Keserű, G. M.; Makara, G. M. Hit Discovery and Hit-to-Lead Approaches. *Drug Discovery Today* **2006**, *11*, 741–748.
- (5) Sun, D.; Gao, W.; Hu, H.; Zhou, S. Why 90% of Clinical Drug Development Fails and How to Improve It? *Acta Pharmaceutica Sinica B* **2022**, *12*, 3049–3062.
- (6) Segall, M. D.; Barber, C. Addressing Toxicity Risk When Designing and Selecting Compounds in Early Drug Discovery. *Drug Discovery Today* **2014**, *19*, 688–693.
- (7) Van Vleet, T. R.; Liguori, M. J.; Lynch, I., James J.; Rao, M.; Warder, S. Screening Strategies and Methods for Better Off-Target Liability Prediction and Identification of Small-Molecule Pharmaceuticals. *SLAS Discovery* **2019**, *24*, 1–24.

- (8) Bleicher, K. H.; Böhm, H.-J.; Müller, K.; Alanine, A. I. Hit and Lead Generation: Beyond High-Throughput Screening. *Nature Reviews Drug Discovery* **2003**, *2*, 369–378.
- (9) Recanatini, M.; Bottegoni, G.; Cavalli, A. In Silico Antitarget Screening. *Drug Discovery Today: Technologies* **2004**, *1*, 209–215.
- (10) Macchiarulo, A.; Nobeli, I.; Thornton, J. M. Ligand Selectivity and Competition Between Enzymes in Silico. *Nature Biotechnology* **2004**, *22*, 1039–1045.
- (11) Elkins, J. M. et al. Comprehensive Characterization of the Published Kinase Inhibitor Set. *Nature Biotechnology* **2016**, *34*, 95–103.
- (12) Raghavendra, N. M.; Pingili, D.; Kadasi, S.; Mettu, A.; Prasad, S. V. U. M. Dual or Multi-Targeting Inhibitors: The Next Generation Anticancer Agents. *European Journal of Medicinal Chemistry* **2018**, *143*, 1277–1300.
- (13) Ibrahim, M. M.; Gabr, M. T. Multitarget Therapeutic Strategies for Alzheimer’s Disease. *Neural Regeneration Research* **2019**, *14*, 437–440.
- (14) Benek, O.; Korabecny, J.; Soukup, O. A Perspective on Multi-target Drugs for Alzheimer’s Disease. *Trends in Pharmacological Sciences* **2020**, *41*, 434–445.
- (15) Brassard, M.; Rondeau, G. Role of Vandetanib in the Management of Medullary Thyroid Cancer. *Biologics : Targets & Therapy* **2012**, *6*, 59–66.
- (16) Okamoto, K.; Ikemori-Kawada, M.; Jestel, A.; von König, K.; Funahashi, Y.; Matsushima, T.; Tsuruoka, A.; Inoue, A.; Matsui, J. Distinct Binding Mode of Multikinase Inhibitor Lenvatinib Revealed by Biochemical Characterization. *ACS Medicinal Chemistry Letters* **2015**, *6*, 89–94.
- (17) Ma, X. H.; Shi, Z.; Tan, C.; Jiang, Y.; Go, M. L.; Low, B. C.; Chen, Y. Z. In-Silico

- Approaches to Multi-target Drug Discovery. *Pharmaceutical Research* **2010**, *27*, 739–749.
- (18) Yousuf, Z.; Iman, K.; Iftikhar, N.; Mirza, M. U. Structure-Based Virtual Screening and Molecular Docking for the Identification of Potential Multi-Targeted Inhibitors Against Breast Cancer. *Breast Cancer: Targets and Therapy* **2017**, *9*, 447–459.
- (19) Chahal, V.; Kakkar, R. A Combination Strategy of Structure-Based Virtual Screening, MM-GBSA, Cross Docking, Molecular Dynamics and Metadynamics Simulations Used to Investigate Natural Compounds as Potent and Specific Inhibitors of Tumor Linked Human Carbonic Anhydrase Ix. *Journal of Biomolecular Structure and Dynamics* **2023**, *41*, 5465–5480.
- (20) Schieferdecker, S.; Vock, E. Development of Pharmacophore Models for the Important Off-Target 5-HT_{2B} Receptor. *Journal of Medicinal Chemistry* **2023**, *66*, 1509–1521.
- (21) Matricon, P.; Nguyen, A. T.; Vo, D. D.; Baltos, J.-A.; Jaiteh, M.; Luttens, A.; Kampen, S.; Christopoulos, A.; Kihlberg, J.; May, L. T.; Carlsson, J. Structure-Based Virtual Screening Discovers Potent and Selective Adenosine A₁ Receptor Antagonists. *European Journal of Medicinal Chemistry* **2023**, *257*, 115419.
- (22) Weiss, D. R.; Karpiak, J.; Huang, X.-P.; Sassano, M. F.; Lyu, J.; Roth, B. L.; Shoichet, B. K. Selectivity Challenges in Docking Screens for GPCR Targets and Antitargets. *Journal of Medicinal Chemistry* **2018**, *61*, 6830–6845.
- (23) Chen, H.; Lyne, P. D.; Giordanetto, F.; Lovell, T.; Li, J. On Evaluating Molecular-Docking Methods for Pose Prediction and Enrichment Factors. *Journal of Chemical Information and Modeling* **2006**, *46*, 401–415.
- (24) Jain, A. N. Bias, Reporting, and Sharing: Computational Evaluations of Docking Methods. *Journal of Computer-Aided Molecular Design* **2008**, *22*, 201–212.

- (25) Cross, J. B.; Thompson, D. C.; Rai, B. K.; Baber, J. C.; Fan, K. Y.; Hu, Y.; Humblet, C. Comparison of Several Molecular Docking Programs: Pose Prediction and Virtual Screening Accuracy. *Journal of Chemical Information and Modeling* **2009**, *49*, 1455–1474.
- (26) Irwin, J. J.; Shoichet, B. K. Docking Screens for Novel Ligands Conferring New Biology. *Journal of Medicinal Chemistry* **2016**, *59*, 4103–4120.
- (27) Boittier, E. D.; Tang, Y. Y.; Buckley, M. E.; Schuurs, Z. P.; Richard, D. J.; Gandhi, N. S. Assessing Molecular Docking Tools to Guide Targeted Drug Discovery of CD38 Inhibitors. *International Journal of Molecular Sciences* **2020**, *21*, 5183.
- (28) Stanzione, F.; Giangreco, I.; Cole, J. C. In *Progress in Medicinal Chemistry*; Witty, D. R., Cox, B., Eds.; Elsevier, 2021; Vol. 60; pp 273–343.
- (29) Ling, L. E. et al. In *Transforming Growth Factor- β in Cancer Therapy, Volume II: Cancer Treatment and Therapy*; Jakowlew, S. B., Ed.; Cancer Drug Discovery and Development; Humana Press: Totowa, NJ, 2008; pp 685–696.
- (30) Bajusz, D.; Ferenczy, G. G.; Keserű, G. M. Discovery of Subtype Selective Janus Kinase (JAK) Inhibitors by Structure-Based Virtual Screening. *Journal of Chemical Information and Modeling* **2016**, *56*, 234–247.
- (31) Lyu, J.; Wang, S.; Balias, T. E.; Singh, I.; Levit, A.; Moroz, Y. S.; O’Meara, M. J.; Che, T.; Algaa, E.; Tolmachova, K.; Tolmachev, A. A.; Shoichet, B. K.; Roth, B. L.; Irwin, J. J. Ultra-Large Library Docking for Discovering New Chemotypes. *Nature* **2019**, *566*, 224–229.
- (32) Gentile, F.; Fernandez, M.; Ban, F.; Ton, A.-T.; Mslati, H.; Perez, C. F.; Leblanc, E.; Yaacoub, J. C.; Gleave, J.; Stern, A.; Wong, B.; Jean, F.; Strynadka, N.; Cherkasov, A. Automated Discovery of Noncovalent Inhibitors of Sars-Cov-2 Main Protease by Con-

- sensus Deep Docking of 40 Billion Small Molecules. *Chemical Science* **2021**, *12*, 15960–15974.
- (33) Alon, A. et al. Structures of the σ_2 Receptor Enable Docking for Bioactive Ligand Discovery. *Nature* **2021**, *600*, 759–764.
- (34) Tingle, B. I.; Irwin, J. J. Large-Scale Docking in the Cloud. *Journal of Chemical Information and Modeling* **2023**, *63*, 2735–2741.
- (35) Garnett, R.; Gärtner, T.; Vogt, M.; Bajorath, J. Introducing the ‘Active Search’ Method for Iterative Virtual Screening. *Journal of Computer-Aided Molecular Design* **2015**, *29*, 305–314.
- (36) Smith, J. S.; Nebgen, B.; Lubbers, N.; Isayev, O.; Roitberg, A. E. Less Is More: Sampling Chemical Space with Active Learning. *The Journal of Chemical Physics* **2018**, *148*, 241733.
- (37) Gentile, F.; Agrawal, V.; Hsing, M.; Ton, A.-T.; Ban, F.; Norinder, U.; Gleave, M. E.; Cherkasov, A. Deep Docking: A Deep Learning Platform for Augmentation of Structure Based Drug Discovery. *ACS Central Science* **2020**, *6*, 939–949.
- (38) Graff, D. E.; Shakhnovich, E. I.; Coley, C. W. Accelerating High-Throughput Virtual Screening Through Molecular Pool-Based Active Learning. *Chemical Science* **2021**, *12*, 7866–7881.
- (39) Yang, Y.; Yao, K.; Repasky, M. P.; Leswing, K.; Abel, R.; Shoichet, B. K.; Jerome, S. V. Efficient Exploration of Chemical Space with Docking and Deep Learning. *Journal of Chemical Theory and Computation* **2021**, *17*, 7106–7119.
- (40) Mehta, S.; Laghuvarapu, S.; Pathak, Y.; Sethi, A.; Alvala, M.; Priyakumar, U. D. MEMES: Machine Learning Framework for Enhanced Molecular Screening. *Chemical Science* **2021**, *12*, 11710–11721.

- (41) Graff, D. E.; Aldeghi, M.; Morrone, J. A.; Jordan, K. E.; Pyzer-Knapp, E. O.; Coley, C. W. Self-Focusing Virtual Screening with Active Design Space Pruning. *Journal of Chemical Information and Modeling* **2022**, *62*, 3854–3862.
- (42) Thompson, J.; Walters, W. P.; Feng, J. A.; Pabon, N. A.; Xu, H.; Maser, M.; Goldman, B. B.; Moustakas, D.; Schmidt, M.; York, F. Optimizing Active Learning for Free Energy Calculations. *Artificial Intelligence in the Life Sciences* **2022**, *2*, 100050.
- (43) Wildman, S. A.; Crippen, G. M. Prediction of Physicochemical Parameters by Atomic Contributions. *Journal of Chemical Information and Computer Sciences* **1999**, *39*, 868–873.
- (44) Ertl, P.; Schuffenhauer, A. Estimation of Synthetic Accessibility Score of Drug-like Molecules Based on Molecular Complexity and Fragment Contributions. *Journal of Cheminformatics* **2009**, *1*, 8.
- (45) Enamine Screening Collections. <https://enamine.net/compound-collections/screening-collection>.
- (46) Fromer, J. C.; Coley, C. W. Computer-Aided Multi-Objective Optimization in Small Molecule Discovery. *Patterns* **2023**, *4*, 100678.
- (47) Janet, J. P.; Ramesh, S.; Duan, C.; Kulik, H. J. Accurate Multiobjective Design in a Space of Millions of Transition Metal Complexes with Neural-Network-Driven Efficient Global Optimization. *ACS Central Science* **2020**, *6*, 513–524.
- (48) Agarwal, G.; Doan, H. A.; Robertson, L. A.; Zhang, L.; Assary, R. S. Discovery of Energy Storage Molecular Materials Using Quantum Chemistry-Guided Multiobjective Bayesian Optimization. *Chemistry of Materials* **2021**, *33*, 8133–8144.
- (49) Gopakumar, A. M.; Balachandran, P. V.; Xue, D.; Gubernatis, J. E.; Lookman, T.

- Multi-objective Optimization for Materials Discovery via Adaptive Design. *Scientific Reports* **2018**, 8, 3738.
- (50) del Rosario, Z.; Rupp, M.; Kim, Y.; Antono, E.; Ling, J. Assessing the Frontier: Active Learning, Model Accuracy, and Multi-Objective Candidate Discovery and Optimization. *The Journal of Chemical Physics* **2020**, 153, 024112.
 - (51) Keane, A. J. Statistical Improvement Criteria for Use in Multiobjective Design Optimization. *AIAA Journal* **2006**, 44, 879–891.
 - (52) Paria, B.; Kandasamy, K.; Póczos, B. A Flexible Framework for Multi-Objective Bayesian Optimization using Random Scalarizations. Proceedings of The 35th Uncertainty in Artificial Intelligence Conference. 2020; pp 766–776.
 - (53) Zhang, R.; Golovin, D. Random Hypervolume Scalarizations for Provable Multi-Objective Black Box Optimization. Proceedings of the 37th International Conference on Machine Learning. 2020; pp 11096–11105.
 - (54) Steuer, R. E.; Choo, E.-U. An Interactive Weighted Tchebycheff Procedure for Multiple Objective Programming. *Mathematical Programming* **1983**, 26, 326–344.
 - (55) Giagkiozis, I.; Fleming, P. J. Methods for Multi-Objective Optimization: An Analysis. *Information Sciences* **2015**, 293, 338–350.
 - (56) Kushner, H. J. A New Method of Locating the Maximum Point of an Arbitrary Multi-peak Curve in the Presence of Noise. *Journal of Basic Engineering* **1964**, 86, 97–106.
 - (57) Moćkus, J. On Bayesian Methods for Seeking the Extremum. Optimization Techniques IFIP Technical Conference Novosibirsk, July 1–7, 1974. Berlin, Heidelberg, 1975; pp 400–404.
 - (58) Srinivas, N.; Krause, A.; Kakade, S. M.; Seeger, M. W. Information-Theoretic Regret

- Bounds for Gaussian Process Optimization in the Bandit Setting. *IEEE Transactions on Information Theory* **2012**, 58, 3250–3265.
- (59) Lin, J. G. In *Directions in Large-Scale Systems: Many-Person Optimization and Decentralized Control*; Ho, Y. C., Mitter, S. K., Eds.; Springer US: Boston, MA, 1976; pp 117–138.
- (60) Hu, Y.; Xian, R.; Wu, Q.; Fan, Q.; Yin, L.; Zhao, H. Revisiting Scalarization in Multi-Task Learning: A Theoretical Perspective. 2023; <http://arxiv.org/abs/2308.13985>.
- (61) Srinivas, N.; Deb, K. Multiobjective Optimization Using Nondominated Sorting in Genetic Algorithms. *Evolutionary Computation* **1994**, 2, 221–248.
- (62) Deb, K.; Pratap, A.; Agarwal, S.; Meyarivan, T. A Fast and Elitist Multiobjective Genetic Algorithm: NSGA-II. *IEEE Transactions on Evolutionary Computation* **2002**, 6, 182–197.
- (63) Drugan, M. M.; Nowe, A. Designing Multi-Objective Multi-Armed Bandits Algorithms: A Study. The 2013 International Joint Conference on Neural Networks (IJCNN). 2013; pp 1–8.
- (64) Gong, T.; Lee, T.; Stephenson, C.; Renduchintala, V.; Padhy, S.; Ndirango, A.; Keskin, G.; Elibol, O. H. A Comparison of Loss Weighting Strategies for Multi task Learning in Deep Neural Networks. *IEEE Access* **2019**, 7, 141627–141632.
- (65) Bellamy, H.; Rehim, A. A.; Orhobor, O. I.; King, R. Batched Bayesian Optimization for Drug Design in Noisy Environments. *Journal of Chemical Information and Modeling* **2022**, 62, 3970–3981.
- (66) Ginsbourger, D.; Le Riche, R.; Carraro, L. In *Computational Intelligence in Expen-*

- sive Optimization Problems*; Tenne, Y., Goh, C.-K., Eds.; Adaptation Learning and Optimization; Springer: Berlin, Heidelberg, 2010; pp 131–162.
- (67) Snoek, J.; Larochelle, H.; Adams, R. P. Practical Bayesian Optimization of Machine Learning Algorithms. *Advances in Neural Information Processing Systems*. 2012.
 - (68) Janusevskis, J.; Le Riche, R.; Ginsbourger, D.; Girdziusas, R. Expected Improvements for the Asynchronous Parallel Global Optimization of Expensive Functions: Potentials and Challenges. *Learning and Intelligent Optimization*. Berlin, Heidelberg, 2012; pp 413–418.
 - (69) Chevalier, C.; Ginsbourger, D. Fast Computation of the Multi-Points Expected Improvement with Applications in Batch Selection. *Learning and Intelligent Optimization*. Berlin, Heidelberg, 2013; pp 59–69.
 - (70) Jiang, S.; Malkomes, G.; Converse, G.; Shofner, A.; Moseley, B.; Garnett, R. Efficient Nonmyopic Active Search. *Proceedings of the 34th International Conference on Machine Learning*. 2017; pp 1714–1723.
 - (71) Tran, A.; Sun, J.; Furlan, J. M.; Pagalthivarthi, K. V.; Visintainer, R. J.; Wang, Y. pBO-2GP-3B: A Batch Parallel Known/Unknown Constrained Bayesian Optimization with Feasibility Classification and Its Applications in Computational Fluid Dynamics. *Computer Methods in Applied Mechanics and Engineering* **2019**, *347*, 827–852.
 - (72) Azimi, J.; Fern, A.; Fern, X. Batch Bayesian Optimization via Simulation Matching. *Advances in Neural Information Processing Systems*. 2010.
 - (73) Gonzalez, J.; Dai, Z.; Hennig, P.; Lawrence, N. Batch Bayesian Optimization via Local Penalization. *Proceedings of the 19th International Conference on Artificial Intelligence and Statistics*. 2016; pp 648–657.

- (74) Konakovic Lukovic, M.; Tian, Y.; Matusik, W. Diversity-Guided Multi-Objective Bayesian Optimization With Batch Evaluations. *Advances in Neural Information Processing Systems*. 2020; pp 17708–17720.
- (75) Citovsky, G.; DeSalvo, G.; Gentile, C.; Karydas, L.; Rajagopalan, A.; Rostamizadeh, A.; Kumar, S. Batch Active Learning at Scale. *Advances in Neural Information Processing Systems*. 2021; pp 11933–11944.
- (76) Maus, N.; Wu, K.; Eriksson, D.; Gardner, J. Discovering Many Diverse Solutions with Bayesian Optimization. *Proceedings of the 26th International Conference on Artificial Intelligence and Statistics (AISTATS)*. Valencia, Spain, 2023.
- (77) González, L. D.; Zavala, V. M. New Paradigms for Exploiting Parallel Experiments in Bayesian Optimization. *Computers & Chemical Engineering* **2023**, *170*, 108110.
- (78) García-Ortegón, M.; Simm, G. N. C.; Tripp, A. J.; Hernández-Lobato, J. M.; Bender, A.; Bacallado, S. DOCKSTRING: Easy Molecular Docking Yields Better Benchmarks for Ligand Design. *Journal of Chemical Information and Modeling* **2022**, *62*, 3486–3502.
- (79) Watson, D. J.; Loiseau, F.; Ingallinesi, M.; Millan, M. J.; Marsden, C. A.; Fone, K. C. Selective Blockade of Dopamine D3 Receptors Enhances while D2 Receptor Antagonism Impairs Social Novelty Discrimination and Novel Object Recognition in Rats: A Key Role for the Prefrontal Cortex. *Neuropsychopharmacology* **2012**, *37*, 770–786.
- (80) Williford, S. E.; Libby, C. J.; Ayokanmbi, A.; Otamias, A.; Gordillo, J. J.; Gordon, E. R.; Cooper, S. J.; Redmann, M.; Li, Y.; Griguer, C.; Zhang, J.; Napierala, M.; Ananthan, S.; Hjelmeland, A. B. Novel Dopamine Receptor 3 Antagonists Inhibit the Growth of Primary and Temozolomide Resistant Glioblastoma Cells. *PLoS ONE* **2021**, *16*, e0250649.

- (81) Bonifazi, A.; Saab, E.; Sanchez, J.; Nazarova, A. L.; Zaidi, S. A.; Jahan, K.; Kattritch, V.; Canals, M.; Lane, J. R.; Newman, A. H. Pharmacological and Physicochemical Properties Optimization for Dual-Target Dopamine D3 (D3R) and μ -Opioid (MOR) Receptor Ligands as Potentially Safer Analgesics. *Journal of Medicinal Chemistry* **2023**,
- (82) Fridman, J. S. et al. Selective Inhibition of JAK1 and JAK2 Is Efficacious in Rodent Models of Arthritis: Preclinical Characterization of INCB028050. *The Journal of Immunology* **2010**, *184*, 5298–5307.
- (83) Liu, Q.; Batt, D. G.; Lippy, J. S.; Surti, N.; Tebben, A. J.; Muckelbauer, J. K.; Chen, L.; An, Y.; Chang, C.; Pokross, M.; Yang, Z.; Wang, H.; Burke, J. R.; Carter, P. H.; Tino, J. A. Design and Synthesis of Carbazole Carboxamides as Promising Inhibitors of Bruton's Tyrosine Kinase (BTK) and Janus Kinase 2 (JAK2). *Bioorganic & Medicinal Chemistry Letters* **2015**, *25*, 4265–4269.
- (84) Li, R.; Pourpak, A.; Morris, S. W. Inhibition of the Insulin-like Growth Factor-1 Receptor (IGF1R) Tyrosine Kinase as a Novel Cancer Therapy Approach. *Journal of Medicinal Chemistry* **2009**, *52*, 4981–5004.
- (85) Pasha, M. K.; Jabeen, I.; Samarasinghe, S. 3D QSAR and Pharmacophore Studies on Inhibitors of Insuline Like Growth Factor 1 Receptor (IGF-1R) and Insulin Receptor (IR) as Potential Anti-Cancer Agents. *Current Research in Chemical Biology* **2022**, *2*, 100019.
- (86) Velaparthi, U.; Liu, P.; Balasubramanian, B.; Carboni, J.; Attar, R.; Gottardis, M.; Li, A.; Greer, A.; Zoeckler, M.; Wittman, M. D.; Vyas, D. Imidazole Moiety Replacements in the 3-(1H-Benzo[d]imidazol-2-Yl)pyridin-2(1H)-One Inhibitors of Insulin-Like Growth Factor Receptor-1 (IGF-1R) to Improve Cytochrome P450 Profile. *Bioorganic & Medicinal Chemistry Letters* **2007**, *17*, 3072–3076.

- (87) Zimmermann, K. et al. Balancing Oral Exposure with CYP3A4 Inhibition in Benzimidazole-Based IGF-IR Inhibitors. *Bioorganic & Medicinal Chemistry Letters* **2008**, *18*, 4075–4080.
- (88) Lin, J. H.; Lu, A. Y. H. Inhibition and Induction of Cytochrome P450 and the Clinical Implications. *Clinical Pharmacokinetics* **1998**, *35*, 361–390.
- (89) Lynch, T.; Price, A. The Effect of Cytochrome P450 Metabolism on Drug Response, Interactions, and Adverse Effects. *American Family Physician* **2007**, *76*, 391–396.
- (90) Cheng, F.; Yu, Y.; Zhou, Y.; Shen, Z.; Xiao, W.; Liu, G.; Li, W.; Lee, P. W.; Tang, Y. Insights into Molecular Basis of Cytochrome P450 Inhibitory Promiscuity of Compounds. *Journal of Chemical Information and Modeling* **2011**, *51*, 2482–2495.
- (91) Yang, K.; Swanson, K.; Jin, W.; Coley, C.; Eiden, P.; Gao, H.; Guzman-Perez, A.; Hopper, T.; Kelley, B.; Mathea, M.; Palmer, A.; Settels, V.; Jaakkola, T.; Jensen, K.; Barzilay, R. Analyzing Learned Molecular Representations for Property Prediction. *Journal of Chemical Information and Modeling* **2019**, *59*, 3370–3388.
- (92) Heid, E.; Greenman, K. P.; Chung, Y.; Li, S.-C.; Graff, D. E.; Vermeire, F. H.; Wu, H.; Green, W. H.; McGill, C. J. Chemprop: A Machine Learning Package for Chemical Property Prediction. 2023; <https://chemrxiv.org/engage/chemrxiv/article-details/64d1f13d4a3f7d0c0dcd836b>.
- (93) Bender, B. J.; Gahbauer, S.; Lutten, A.; Lyu, J.; Webb, C. M.; Stein, R. M.; Fink, E. A.; Balius, T. E.; Carlsson, J.; Irwin, J. J.; Shoichet, B. K. A Practical Guide to Large-Scale Docking. *Nature Protocols* **2021**, *16*, 4799–4832.
- (94) Bemis, G. W.; Murcko, M. A. The Properties of Known Drugs. 1. Molecular Frameworks. *Journal of Medicinal Chemistry* **1996**, *39*, 2887–2893.

- (95) McInnes, L.; Healy, J.; Saul, N.; Großberger, L. UMAP: Uniform Manifold Approximation and Projection. *Journal of Open Source Software* **2018**, *3*, 861.
- (96) Tandon, R. et al. RBx10080307, a Dual EGFR/IGF-1R Inhibitor for Anticancer Therapy. *European Journal of Pharmacology* **2013**, *711*, 19–26.
- (97) Hu, L.; Fan, M.; Shi, S.; Song, X.; Wang, F.; He, H.; Qi, B. Dual Target Inhibitors Based on EGFR: Promising Anticancer Agents for the Treatment of Cancers (2017-). *European Journal of Medicinal Chemistry* **2022**, *227*, 113963.
- (98) Kang, J.; Guo, Z.; Zhang, H.; Guo, R.; Zhu, X.; Guo, X. Dual Inhibition of EGFR and IGF-1R Signaling Leads to Enhanced Antitumor Efficacy against Esophageal Squamous Cancer. *International Journal of Molecular Sciences* **2022**, *23*, 10382.
- (99) Abourehab, M. A. S.; Alqahtani, A. M.; Youssif, B. G. M.; Gouda, A. M. Globally Approved EGFR Inhibitors: Insights into Their Syntheses, Target Kinases, Biological Activities, Receptor Interactions, and Metabolism. *Molecules* **2021**, *26*, 6677.
- (100) Pan, Y.; Huang, N.; Cho, S.; MacKerell, A. D. Consideration of molecular weight during compound selection in virtual target-based database screening. *Journal of Chemical Information and Computer Sciences* **2003**, *43*, 267–272.
- (101) Li, H.; Zhang, H.; Zheng, M.; Luo, J.; Kang, L.; Liu, X.; Wang, X.; Jiang, H. An effective docking strategy for virtual screening based on multi-objective optimization algorithm. *BMC Bioinformatics* **2009**, *10*, 58.
- (102) Kirsch, A.; van Amersfoort, J.; Gal, Y. BatchBALD: Efficient and Diverse Batch Acquisition for Deep Bayesian Active Learning. *Advances in Neural Information Processing Systems*. 2019.
- (103) Huggins, D. J.; Sherman, W.; Tidor, B. Rational Approaches to Improving Selectivity in Drug Design. *Journal of Medicinal Chemistry* **2012**, *55*, 1424–1444.

- (104) Klabunde, T.; Evers, A. GPCR Antitarget Modeling: Pharmacophore Models for Biogenic Amine Binding GPCRs to Avoid GPCR-Mediated Side Effects. *ChemBioChem* **2005**, *6*, 876–889.
- (105) RDKit: Open-Source Cheminformatics Software. <http://www.rdkit.org/>.
- (106) Motoyama, Y.; Tamura, R.; Yoshimi, K.; Terayama, K.; Ueno, T.; Tsuda, K. Bayesian Optimization Package: PHYSBO. *Computer Physics Communications* **2022**, *278*, 108405.
- (107) Couckuyt, I.; Deschrijver, D.; Dhaene, T. Fast Calculation of Multiobjective Probability of Improvement and Expected Improvement Criteria for Pareto Optimization. *Journal of Global Optimization* **2014**, *60*, 575–594.
- (108) Biscani, F.; Izzo, D. A Parallel Global Multiobjective Framework for Optimization: Pagmo. *Journal of Open Source Software* **2020**, *5*, 2338.
- (109) Paszke, A. et al. PyTorch: An Imperative Style, High-Performance Deep Learning Library. *Advances in Neural Information Processing Systems*. 2019.
- (110) Nix, D.; Weigend, A. Estimating the Mean and Variance of the Target Probability Distribution. *Proceedings of 1994 IEEE International Conference on Neural Networks (ICNN'94)*. 1994; pp 55–60 vol.1.
- (111) Hirschfeld, L.; Swanson, K.; Yang, K.; Barzilay, R.; Coley, C. W. Uncertainty Quantification Using Neural Networks for Molecular Property Prediction. *Journal of Chemical Information and Modeling* **2020**, *60*, 3770–3780.
- (112) Carhart, R. E.; Smith, D. H.; Venkataraghavan, R. Atom Pairs as Molecular Features in Structure-Activity Studies: Definition and Applications. *Journal of Chemical Information and Computer Sciences* **1985**, *25*, 64–73.

- (113) Awale, M.; Reymond, J.-L. Atom Pair 2D-Fingerprints Perceive 3D-Molecular Shape and Pharmacophores for Very Fast Virtual Screening of ZINC and GDB-17. *Journal of Chemical Information and Modeling* **2014**, *54*, 1892–1907.
- (114) O’Boyle, N. M.; Sayle, R. A. Comparing structural fingerprints using a literature-based similarity benchmark. *Journal of Cheminformatics* **2016**, *8*, 36.
- (115) Sculley, D. Web-Scale k-Means Clustering. Proceedings of the 19th international conference on World wide web. Raleigh North Carolina USA, 2010; pp 1177–1178.
- (116) Pedregosa, F. et al. Scikit-learn: Machine Learning in Python. *Journal of Machine Learning Research* **2011**, *12*, 2825–2830.
- (117) Tanabe, R.; Ishibuchi, H. An Analysis of Quality Indicators Using Approximated Optimal Distributions in a 3-D Objective Space. *IEEE Transactions on Evolutionary Computation* **2020**, *24*, 853–867.
- (118) Bosman, P.; Thierens, D. The Balance Between Proximity and Diversity in Multi-objective Evolutionary Algorithms. *IEEE Transactions on Evolutionary Computation* **2003**, *7*, 174–188.
- (119) Blank, J.; Deb, K. Pymoo: Multi-Objective Optimization in Python. *IEEE Access* **2020**, *8*, 89497–89509.
- (120) Reuther, A. et al. Interactive Supercomputing on 40,000 Cores for Machine Learning and Data Analysis. 2018 IEEE High Performance extreme Computing Conference (HPEC). 2018; pp 1–6.

Supporting Information:

Pareto Optimization to Accelerate Multi-Objective Virtual Screening

Jenna C. Fromer,[†] David E. Graff,^{†,‡} and Connor W. Coley^{*,†,¶}

[†]*Department of Chemical Engineering, MIT, Cambridge, MA 02139*

[‡]*Department of Chemistry and Chemical Biology, Harvard University, Cambridge, MA
02138*

[¶]*Department of Electrical Engineering and Computer Science, MIT, Cambridge, MA 02139*

E-mail: ccoley@mit.edu

S1 Model-guided Optimization Algorithms

Algorithm S1: Multi-objective Bayesian optimization using scalarization

Input: Objective function $\mathbf{f} : x \mapsto \mathbb{R}^N$, weight vector $\boldsymbol{\lambda} = [\lambda_1, \dots, \lambda_N]$, surrogate model \hat{f} , candidate set \mathcal{X} , acquisition function $\alpha : x \mapsto \mathbb{R}$, initial observation size b_0 , batch size b

- 1 Select random subset of design space: $\mathcal{X}_0 \subset \mathcal{X} : |\mathcal{X}_0| = b_0$
- 2 Initialize dataset: $\mathcal{D}_0 \leftarrow \{(x, \boldsymbol{\lambda} \cdot \mathbf{f}(x)) : x \in \mathcal{X}_0\}$
- 3 **for** $t \leftarrow 1 \dots T$ **do**
- 4 Train \hat{f} on \mathcal{D}_{t-1}
- 5 Select new batch: $\mathcal{X}_t \leftarrow \arg \max_{\mathcal{X}_t \subset \mathcal{X} : |\mathcal{X}_t| = b} \sum_{x \in \mathcal{X}_t} \alpha(x; \hat{f}, \mathcal{D}_{t-1})$
- 6 Update dataset: $\mathcal{D}_t \leftarrow \mathcal{D}_{t-1} \cup \{(x, \boldsymbol{\lambda} \cdot \mathbf{f}(x)) : x \in \mathcal{X}_t\}$
- 7 **end**

Output: $\arg \max_{x \in \mathcal{D}_T} \boldsymbol{\lambda} \cdot \mathbf{f}(x)$

Algorithm S2: Multi-objective Bayesian optimization using Pareto optimization

Input: Objective function $\mathbf{f} : x \mapsto \mathbb{R}^N$, surrogate models $\{\hat{f}^{(n)}\}_{n=1}^N$, candidate set \mathcal{X} , acquisition function $\alpha : x \mapsto \mathbb{R}$, initial observation size b_0 , batch size b

- 1 Select random subset of design space: $\mathcal{X}_0 \subset \mathcal{X} : |\mathcal{X}_0| = b_0$
- 2 Initialize dataset: $\mathcal{D}_0 \leftarrow \{(x, \mathbf{f}(x)) : x \in \mathcal{X}_0\}$
- 3 Calculate Pareto front: $\mathcal{P}_0 \leftarrow \text{pareto_front}(\mathcal{D}_0)$
- 4 **for** $t \leftarrow 1 \dots T$ **do**
- 5 **for** $n \leftarrow 1 \dots N$ **do**
- 6 Train $\hat{f}^{(n)}$ on $\{(x, f_n) : x, \mathbf{f}(x) \in \mathcal{D}_{t-1}\}$
- 7 **end**
- 8 Select new batch: $\mathcal{X}_t \leftarrow \arg \max_{\mathcal{X}_t \subset \mathcal{X} : |\mathcal{X}_t| = b} \sum_{x \in \mathcal{X}_t} \alpha(x; \{\hat{f}^{(n)}\}, \mathcal{D}_{t-1}, \mathcal{P}_{t-1})$
- 9 Update dataset: $\mathcal{D}_t \leftarrow \mathcal{D}_{t-1} \cup \{(x, \mathbf{f}(x)) : x \in \mathcal{X}_t\}$
- 10 Update Pareto front: $\mathcal{P}_t \leftarrow \text{pareto_front}(\mathcal{D}_t)$
- 11 **end**

Output: \mathcal{P}_T

S2 Performance Metrics

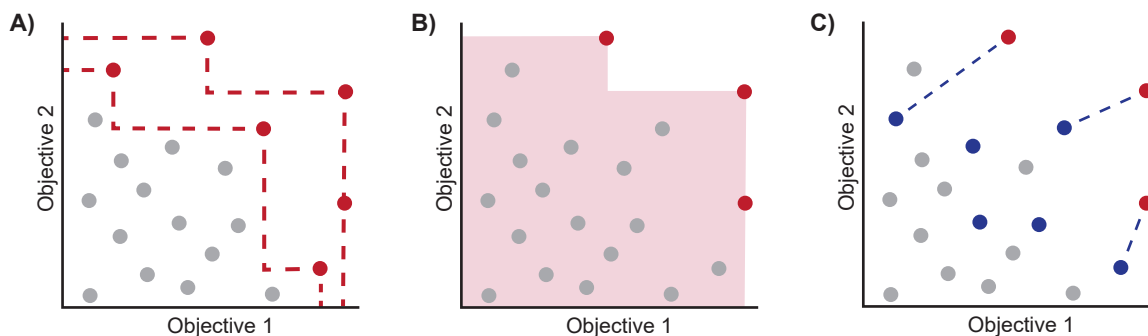


Figure S1: Illustration of the Pareto optimization evaluation metrics considered in this work. (A) Definition of true top- k molecules through non-dominated sorting. Here, the top 30% are shown in red. (B) Hypervolume metric. (C) Inverted generation distance, which averages the shortest distance between points on the true Pareto front (red) and acquired points (blue).

S3 Comparison of Acquisition Functions

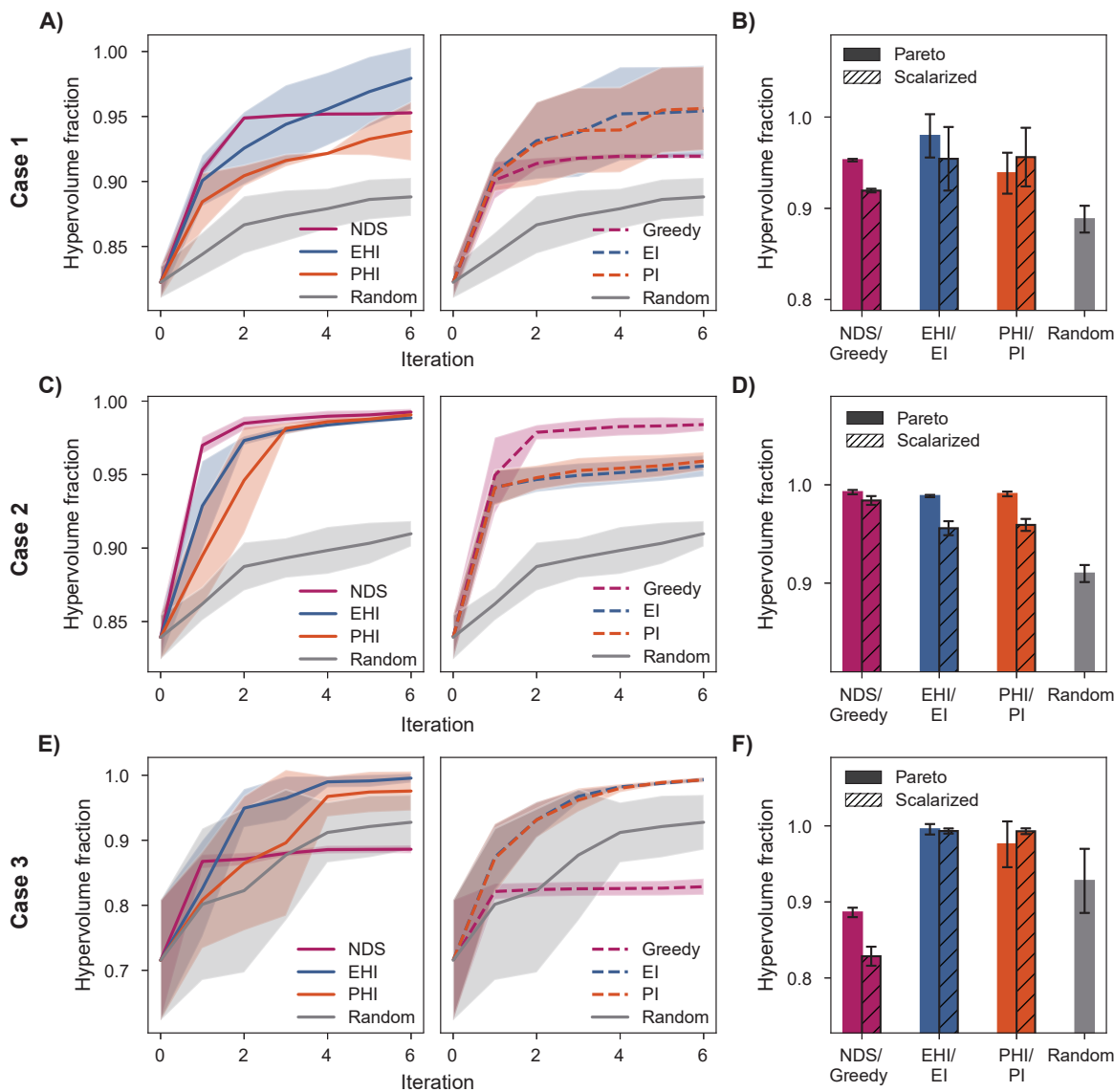


Figure S2: Fraction of hypervolume acquired across iterations (A, C, E) and after six iterations (B, D, F) for three case studies. All cases minimized docking scores to one target and maximized docking scores to one off-target. Cases 1, 2, and 3 aimed to identify putative selective inhibitors of DRD3 over DRD2, JAK2 over LCK, and IGF1R over CYP3A4, respectively. Docking scores to all targets were extracted from the published DOCKSTRING dataset of 260k molecules.^{S1} 1% of the virtual library was acquired at each iteration using top-k batching. Error bars (B, D, F) and shaded regions (A, C, E) denote \pm one standard deviation across five runs.

S4 Molecular Diversity Visualization

2-dimensional projections of molecular fingerprints can illustrate molecular diversity in a qualitative sense. We use UMAP projections^{S2} to visualize the improvement in molecular diversity of acquired points with diversity-enhanced acquisition strategies. Figure S3 shows UMAP projections of acquired points at iterations 1, 3, and 5 for single experiments using different diversity-enhancing acquisition strategies. These experiments were for the identification of putative IGF1R inhibitors with selectivity over CYP3A4. UMAP embeddings were trained on the entire searched library, shown as blue density plots. Diversity is compared for acquisition that implements no clustering, clustering in the feature space, clustering in the objective space, and clustering in both spaces. The acquired molecules (red points) are qualitatively more dispersed across the chemical space spanned by the library when compared to the points acquired without clustering. While the visualization of molecular diversity through dimensional reduction is qualitative in nature, the difference in the chemical space acquired in the two runs suggests that diversity-enhanced acquisition improves the structural diversity of acquired points.

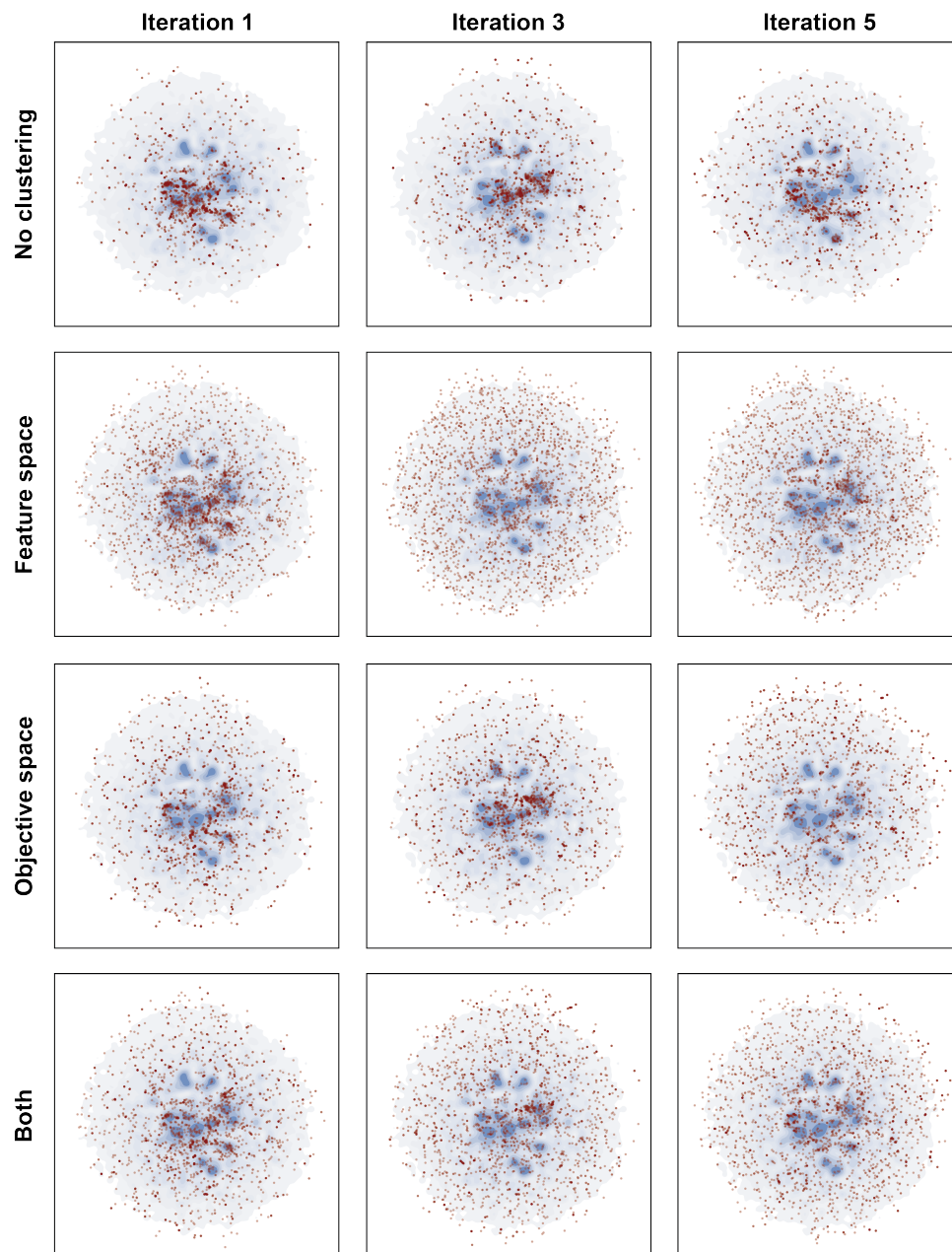


Figure S3: UMAP projections demonstrating molecular diversity of acquired points using standard and diversity-enhanced acquisition. Each row is a single run using the specified diversity-enhanced acquisition strategy with PHI. The runs corresponding to each row were initialized with the same random set of acquired points at iteration 0 and the same model seed. Docking scores computed with DOCKSTRING^{S1} to IGF1R and CYP3A4 were minimized and maximized, respectively, to identify putative selective inhibitors of IGF1R. Points acquired at iterations 1, 3, and 5 are shown for the four acquisition strategies tested in red. UMAP projections were trained on the entire virtual library (shown as a blue density behind acquired points).

S5 Large-Scale Multi-Objective Screen Results

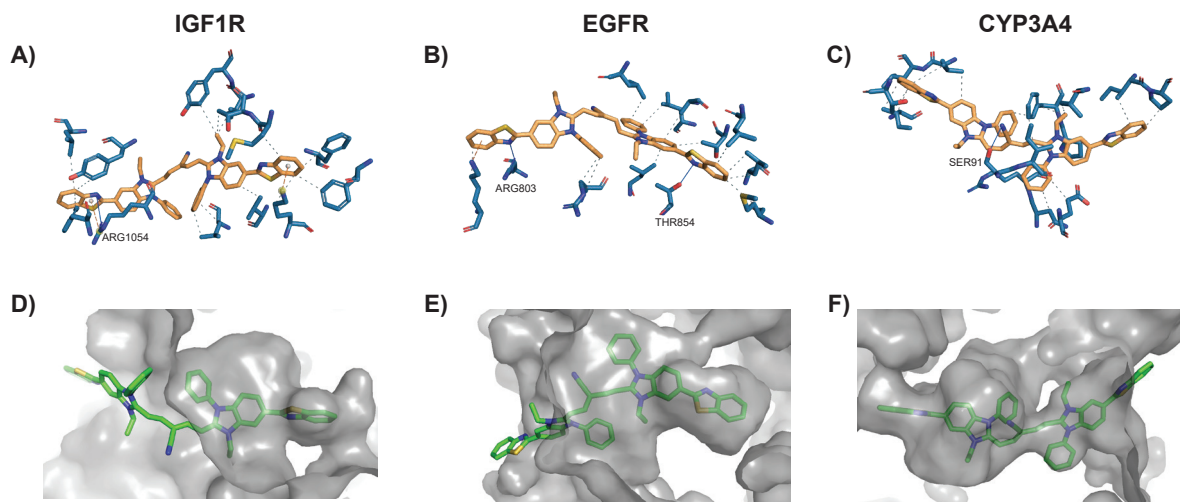


Figure S4: Docking poses of one non-dominated molecule (M2) predicted to selectively bind IGF1R and EGFR over CYP3A4. Docking poses were computed with DOCKSTRING,^{S1} an AutoDock Vina wrapper with prepared docking settings for IGF1R, EGFR, and CYP3A4. The Enamine screening database^{S3} of over 4M molecules was used as the virtual library. (A-C) Protein-ligand interactions of M2 with IGF1R, EGFR, and CYP3A4 prepared with PLIP.^{S4} (D-F) Space-filling visualization of M2 in the binding pockets of IGF1R, EGFR, and CYP3A4. The docking-based optimization for predicted selectivity favors bulky molecules like M2 that can fit in the binding pockets of targets IGF1R and EGFR but form unresolvable steric clashes with residues that form the pocket of off-target CYP3A4.

ID	Structure	Scores	ID	Structure	Scores
M0		IGF1R: -8.4 EGFR: -12.7 CYP3A4: -8.3	M8		IGF1R: -10.2 EGFR: -13.5 CYP3A4: -11.8
M1		IGF1R: -9.2 EGFR: -12.5 CYP3A4: -8.0	M9		IGF1R: -10.4 EGFR: -12.2 CYP3A4: -9.1
M2		IGF1R: -9.3 EGFR: -11.9 CYP3A4: -2.8	M10		IGF1R: -10.5 EGFR: -13.4 CYP3A4: -11.2
M3		IGF1R: -9.5 EGFR: -14.1 CYP3A4: -12.1	M11		IGF1R: -10.5 EGFR: -13.7 CYP3A4: -12.1
M4		IGF1R: -9.5 EGFR: -11.6 CYP3A4: 0	M12		IGF1R: -10.9 EGFR: -13.3 CYP3A4: -9.6
M5		IGF1R: -9.7 EGFR: -12.1 CYP3A4: -7.3	M13		IGF1R: -11.1 EGFR: -14.2 CYP3A4: -12.7
M6		IGF1R: -10 EGFR: -13.8 CYP3A4: -11.9	M14		IGF1R: -11.1 EGFR: -13 CYP3A4: -11.9
M7		IGF1R: -10.2 EGFR: -13.2 CYP3A4: -8.5	M15		IGF1R: -11.1 EGFR: -12.5 CYP3A4: -9.3

Figure S5: Molecules 0-15 of the 39 non-dominated molecules for an exemplary 3-objective optimization aiming to identify binders of IGF1R and EGFR with selectivity over CYP3A4 from the Enamine screening library of over 4M molecules.^{S3} Docking scores were computed using DOCKSTRING.^{S1} Docking scores to IGF1R and EGFR were minimized, and scores to the off-target CYP3A4 were maximized.

ID	Structure	Scores	ID	Structure	Scores
M16		IGF1R: -11.2 EGFR: -12.2 CYP3A4: -9.9	M24		IGF1R: -11.6 EGFR: -11.8 CYP3A4: -9.1
M17		IGF1R: -11.2 EGFR: -12.2 CYP3A4: -9.9	M25		IGF1R: -11.6 EGFR: -13.3 CYP3A4: -12.2
M18		IGF1R: -11.2 EGFR: -12.6 CYP3A4: -10.3	M26		IGF1R: -11.6 EGFR: -12.5 CYP3A4: -11.3
M19		IGF1R: -11.3 EGFR: -12.2 CYP3A4: -11.1	M27		IGF1R: -11.8 EGFR: -12.1 CYP3A4: -11.7
M20		IGF1R: -11.3 EGFR: -12 CYP3A4: -4.3	M28		IGF1R: -11.9 EGFR: -11.3 CYP3A4: -10.5
M21		IGF1R: -11.4 EGFR: -12.9 CYP3A4: -11.6	M29		IGF1R: -11.9 EGFR: -11.9 CYP3A4: -11
M22		IGF1R: -11.4 EGFR: -13.8 CYP3A4: -13.2	M30		IGF1R: -11.9 EGFR: -12.3 CYP3A4: -12.1
M23		IGF1R: -11.6 EGFR: -12.9 CYP3A4: -12	M31		IGF1R: -12 EGFR: -11.1 CYP3A4: -11.3

Figure S6: Molecules 16-31 of the 39 non-dominated molecules in the searched library for an exemplary 3-objective optimization aiming to identify binders of IGF1R and EGFR with selectivity over CYP3A4 from the Enamine screening library of over 4M molecules.^{S3} Docking scores were computed using DOCKSTRING.^{S1} Docking scores to IGF1R and EGFR were minimized, and scores to the off-target CYP3A4 were maximized.

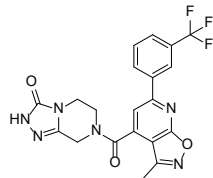
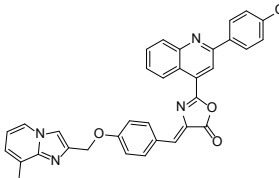
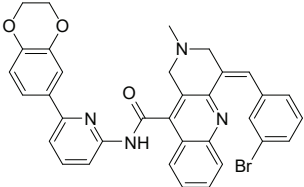
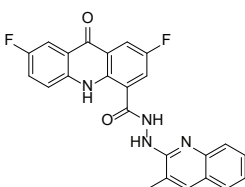
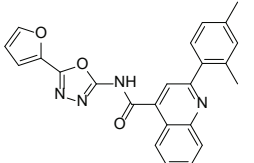
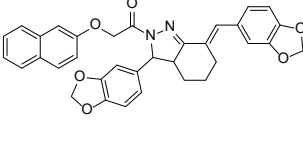
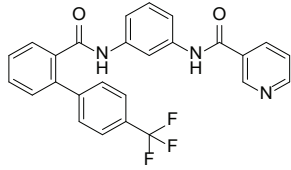
ID	Structure	Scores	ID	Structure	Scores
M32		IGF1R: -12.1 EGFR: -11.4 CYP3A4: -11.4	M36		IGF1R: -12.5 EGFR: -12.9 CYP3A4: -13.1
M33		IGF1R: -12.1 EGFR: -13.6 CYP3A4: -12.6	M37		IGF1R: -12.5 EGFR: -12.7 CYP3A4: -12.2
M34		IGF1R: -12.1 EGFR: -11.5 CYP3A4: -11.6	M38		IGF1R: -13 EGFR: -12 CYP3A4: -12.6
M35		IGF1R: -12.2 EGFR: -10.6 CYP3A4: -11.3			

Figure S7: Molecules 32-38 of the 39 non-dominated molecules in the searched library for an exemplary 3-objective optimization aiming to identify binders of IGF1R and EGFR with selectivity over CYP3A4 from the Enamine screening library of over 4M molecules.^{S3} Docking scores were computed using DOCKSTRING.^{S1} Docking scores to IGF1R and EGFR were minimized, and scores to the off-target CYP3A4 were maximized.

S6 Tables

Table S1: Fraction of top-1% acquired across iterations for retrospective multi-objective virtual screening experiments in Section 3.2, shown in Figure 4. All cases minimized docking scores to one target and maximized docking scores to one off-target. Cases 1, 2, and 3 aimed to identify putative selective inhibitors of DRD3 over DRD2, JAK2 over LCK, and IGF1R over CYP3A4, respectively. Docking scores to all targets were extracted from the published DOCKSTRING dataset of 260k molecules.^{S1} 1% of the virtual library was acquired at each iteration using top-k batching. Means \pm one standard deviation across 5 trials are shown.

Case	Acquisition Function	0	1	2	Iteration 3	4	5	6
1	EHI	0.01 \pm 0.00	0.15 \pm 0.01	0.21 \pm 0.03	0.25 \pm 0.03	0.30 \pm 0.02	0.33 \pm 0.02	0.36 \pm 0.02
1	EI	0.01 \pm 0.00	0.14 \pm 0.02	0.17 \pm 0.02	0.20 \pm 0.02	0.23 \pm 0.02	0.25 \pm 0.02	0.27 \pm 0.02
1	Greedy	0.01 \pm 0.00	0.17 \pm 0.01	0.25 \pm 0.01	0.31 \pm 0.02	0.36 \pm 0.01	0.41 \pm 0.01	0.45 \pm 0.01
1	NDS	0.01 \pm 0.00	0.16 \pm 0.02	0.25 \pm 0.01	0.30 \pm 0.01	0.34 \pm 0.01	0.37 \pm 0.01	0.40 \pm 0.01
1	PHI	0.01 \pm 0.00	0.17 \pm 0.01	0.25 \pm 0.02	0.31 \pm 0.02	0.36 \pm 0.02	0.40 \pm 0.01	0.43 \pm 0.01
1	PI	0.01 \pm 0.00	0.14 \pm 0.02	0.18 \pm 0.02	0.21 \pm 0.01	0.24 \pm 0.02	0.27 \pm 0.02	0.29 \pm 0.02
1	Random	0.01 \pm 0.00	0.02 \pm 0.00	0.03 \pm 0.00	0.04 \pm 0.00	0.05 \pm 0.01	0.06 \pm 0.01	0.07 \pm 0.01
2	EHI	0.01 \pm 0.00	0.13 \pm 0.04	0.15 \pm 0.04	0.17 \pm 0.03	0.20 \pm 0.03	0.23 \pm 0.04	0.25 \pm 0.04
2	EI	0.01 \pm 0.00	0.03 \pm 0.00	0.03 \pm 0.00	0.04 \pm 0.00	0.05 \pm 0.00	0.07 \pm 0.00	0.08 \pm 0.00
2	Greedy	0.01 \pm 0.00	0.09 \pm 0.03	0.13 \pm 0.03	0.16 \pm 0.04	0.20 \pm 0.04	0.22 \pm 0.04	0.25 \pm 0.04
2	NDS	0.01 \pm 0.00	0.13 \pm 0.01	0.21 \pm 0.01	0.26 \pm 0.01	0.29 \pm 0.01	0.32 \pm 0.01	0.34 \pm 0.01
2	PHI	0.01 \pm 0.00	0.18 \pm 0.02	0.21 \pm 0.02	0.25 \pm 0.02	0.28 \pm 0.01	0.31 \pm 0.00	0.35 \pm 0.02
2	PI	0.01 \pm 0.00	0.03 \pm 0.00	0.04 \pm 0.00	0.05 \pm 0.00	0.06 \pm 0.00	0.07 \pm 0.01	0.08 \pm 0.00
2	Random	0.01 \pm 0.00	0.02 \pm 0.00	0.03 \pm 0.00	0.04 \pm 0.00	0.05 \pm 0.00	0.06 \pm 0.00	0.07 \pm 0.00
3	EHI	0.01 \pm 0.00	0.04 \pm 0.01	0.06 \pm 0.01	0.11 \pm 0.01	0.17 \pm 0.02	0.23 \pm 0.01	0.26 \pm 0.01
3	EI	0.01 \pm 0.00	0.03 \pm 0.01	0.04 \pm 0.01	0.05 \pm 0.01	0.06 \pm 0.01	0.08 \pm 0.01	0.09 \pm 0.01
3	Greedy	0.01 \pm 0.00	0.03 \pm 0.00	0.06 \pm 0.00	0.08 \pm 0.00	0.11 \pm 0.01	0.13 \pm 0.01	0.15 \pm 0.01
3	NDS	0.01 \pm 0.00	0.05 \pm 0.01	0.08 \pm 0.00	0.12 \pm 0.01	0.15 \pm 0.01	0.17 \pm 0.01	0.19 \pm 0.01
3	PHI	0.01 \pm 0.00	0.03 \pm 0.01	0.07 \pm 0.02	0.11 \pm 0.03	0.17 \pm 0.04	0.24 \pm 0.04	0.28 \pm 0.03
3	PI	0.01 \pm 0.00	0.03 \pm 0.01	0.04 \pm 0.01	0.05 \pm 0.01	0.06 \pm 0.01	0.07 \pm 0.00	0.09 \pm 0.00
3	Random	0.01 \pm 0.00	0.02 \pm 0.00	0.03 \pm 0.00	0.04 \pm 0.00	0.05 \pm 0.00	0.06 \pm 0.00	0.07 \pm 0.00

Table S2: Hypervolume profiles for retrospective multi-objective virtual screening experiments in Section 3.2, shown in Figure S2. All cases minimized docking scores to one target and maximized docking scores to one off-target. Cases 1, 2, and 3 aimed to identify putative selective inhibitors of DRD3 over DRD2, JAK2 over LCK, and IGF1R over CYP3A4, respectively. Docking scores to all targets were extracted from the published DOCKSTRING dataset of 260k molecules.^{S1} 1% of the virtual library was acquired at each iteration using top-k batching. Means \pm one standard deviation across 5 trials are shown.

Case	Acquisition Function	Iteration						
		0	1	2	3	4	5	6
1	EHI	0.82 \pm 0.01	0.90 \pm 0.02	0.93 \pm 0.03	0.94 \pm 0.03	0.96 \pm 0.03	0.97 \pm 0.03	0.98 \pm 0.02
1	EI	0.82 \pm 0.01	0.91 \pm 0.01	0.93 \pm 0.03	0.94 \pm 0.03	0.95 \pm 0.04	0.95 \pm 0.04	0.95 \pm 0.03
1	Greedy	0.82 \pm 0.01	0.90 \pm 0.01	0.91 \pm 0.00	0.92 \pm 0.00	0.92 \pm 0.00	0.92 \pm 0.00	0.92 \pm 0.00
1	NDS	0.82 \pm 0.01	0.91 \pm 0.00	0.95 \pm 0.00	0.95 \pm 0.00	0.95 \pm 0.00	0.95 \pm 0.00	0.95 \pm 0.00
1	PHI	0.82 \pm 0.01	0.88 \pm 0.02	0.90 \pm 0.01	0.92 \pm 0.00	0.92 \pm 0.00	0.93 \pm 0.01	0.94 \pm 0.02
1	PI	0.82 \pm 0.01	0.91 \pm 0.01	0.93 \pm 0.03	0.94 \pm 0.03	0.94 \pm 0.03	0.95 \pm 0.03	0.96 \pm 0.03
1	Random	0.82 \pm 0.01	0.84 \pm 0.02	0.87 \pm 0.02	0.87 \pm 0.02	0.88 \pm 0.02	0.89 \pm 0.02	0.89 \pm 0.01
2	EHI	0.84 \pm 0.01	0.93 \pm 0.03	0.97 \pm 0.00	0.98 \pm 0.00	0.98 \pm 0.00	0.99 \pm 0.00	0.99 \pm 0.00
2	EI	0.84 \pm 0.01	0.94 \pm 0.01	0.95 \pm 0.01	0.95 \pm 0.01	0.95 \pm 0.01	0.95 \pm 0.01	0.96 \pm 0.01
2	Greedy	0.84 \pm 0.01	0.95 \pm 0.03	0.98 \pm 0.00	0.98 \pm 0.01	0.98 \pm 0.01	0.98 \pm 0.01	0.98 \pm 0.00
2	NDS	0.84 \pm 0.01	0.97 \pm 0.01	0.98 \pm 0.00	0.99 \pm 0.00	0.99 \pm 0.00	0.99 \pm 0.00	0.99 \pm 0.00
2	PHI	0.84 \pm 0.01	0.89 \pm 0.03	0.95 \pm 0.04	0.98 \pm 0.00	0.99 \pm 0.00	0.99 \pm 0.00	0.99 \pm 0.00
2	PI	0.84 \pm 0.01	0.94 \pm 0.01	0.95 \pm 0.01	0.95 \pm 0.01	0.95 \pm 0.01	0.96 \pm 0.01	0.96 \pm 0.01
2	Random	0.84 \pm 0.01	0.86 \pm 0.01	0.89 \pm 0.02	0.89 \pm 0.01	0.90 \pm 0.02	0.90 \pm 0.01	0.91 \pm 0.01
3	EHI	0.72 \pm 0.09	0.83 \pm 0.07	0.95 \pm 0.03	0.96 \pm 0.03	0.99 \pm 0.01	0.99 \pm 0.01	1.00 \pm 0.01
3	EI	0.72 \pm 0.09	0.87 \pm 0.05	0.93 \pm 0.03	0.97 \pm 0.01	0.98 \pm 0.00	0.99 \pm 0.00	0.99 \pm 0.00
3	Greedy	0.72 \pm 0.09	0.82 \pm 0.01	0.82 \pm 0.01	0.83 \pm 0.01	0.83 \pm 0.01	0.83 \pm 0.01	0.83 \pm 0.01
3	NDS	0.72 \pm 0.09	0.87 \pm 0.01	0.87 \pm 0.01	0.88 \pm 0.00	0.89 \pm 0.01	0.89 \pm 0.01	0.89 \pm 0.01
3	PHI	0.72 \pm 0.09	0.81 \pm 0.07	0.86 \pm 0.10	0.90 \pm 0.11	0.97 \pm 0.03	0.97 \pm 0.03	0.98 \pm 0.03
3	PI	0.72 \pm 0.09	0.87 \pm 0.05	0.93 \pm 0.03	0.96 \pm 0.02	0.98 \pm 0.01	0.99 \pm 0.00	0.99 \pm 0.00
3	Random	0.72 \pm 0.09	0.80 \pm 0.12	0.82 \pm 0.13	0.88 \pm 0.10	0.91 \pm 0.05	0.92 \pm 0.05	0.93 \pm 0.04

Table S3: Comparison of acquisition functions using all four evaluation metrics after a fixed exploration budget of 6 iterations. Top-1%, hypervolume (HV), inverted generational distance (IGD), and fraction of the true Pareto front are shown. Values are plotted in Figures 4, 5, and S2. All cases minimized docking scores to one target and maximized docking scores to one off-target. Cases 1, 2, and 3 aimed to identify putative selective inhibitors of DRD3 over DRD2, JAK2 over LCK, and IGF1R over CYP3A4, respectively. Docking scores to all targets were extracted from the published DOCKSTRING dataset of 260k molecules.^{S1} 1% of the virtual library was acquired at each iteration using top-k batching. Means \pm one standard deviation across 5 trials are shown.

Case	Acquisition Function	Top 1%	HV	IGD	Fraction of True Front
1	EHI	0.36 ± 0.02	0.98 ± 0.02	0.11 ± 0.06	0.68 ± 0.05
1	EI	0.27 ± 0.02	0.95 ± 0.03	0.22 ± 0.12	0.52 ± 0.06
1	Greedy	0.45 ± 0.01	0.92 ± 0.00	0.33 ± 0.01	0.51 ± 0.02
1	NDS	0.40 ± 0.01	0.95 ± 0.00	0.20 ± 0.01	0.49 ± 0.04
1	PHI	0.43 ± 0.01	0.94 ± 0.02	0.23 ± 0.06	0.61 ± 0.03
1	PI	0.29 ± 0.02	0.96 ± 0.03	0.21 ± 0.11	0.53 ± 0.07
1	Random	0.07 ± 0.01	0.89 ± 0.01	0.62 ± 0.04	0.09 ± 0.04
2	EHI	0.25 ± 0.04	0.99 ± 0.00	0.10 ± 0.01	0.41 ± 0.03
2	EI	0.08 ± 0.00	0.96 ± 0.01	0.28 ± 0.03	0.20 ± 0.05
2	Greedy	0.25 ± 0.04	0.98 ± 0.00	0.10 ± 0.02	0.38 ± 0.05
2	NDS	0.34 ± 0.01	0.99 ± 0.00	0.07 ± 0.02	0.48 ± 0.05
2	PHI	0.35 ± 0.02	0.99 ± 0.00	0.08 ± 0.01	0.47 ± 0.03
2	PI	0.08 ± 0.00	0.96 ± 0.01	0.28 ± 0.01	0.21 ± 0.03
2	Random	0.07 ± 0.00	0.91 ± 0.01	0.31 ± 0.03	0.03 ± 0.03
3	EHI	0.26 ± 0.01	1.00 ± 0.01	0.07 ± 0.07	0.82 ± 0.10
3	EI	0.09 ± 0.01	0.99 ± 0.00	0.18 ± 0.07	0.62 ± 0.10
3	Greedy	0.15 ± 0.01	0.83 ± 0.01	1.25 ± 0.09	0.02 ± 0.04
3	NDS	0.19 ± 0.01	0.89 ± 0.01	0.74 ± 0.03	0.24 ± 0.08
3	PHI	0.28 ± 0.03	0.98 ± 0.03	0.19 ± 0.15	0.72 ± 0.15
3	PI	0.09 ± 0.00	0.99 ± 0.00	0.21 ± 0.08	0.60 ± 0.11
3	Random	0.07 ± 0.00	0.93 ± 0.04	0.76 ± 0.22	0.16 ± 0.12

Table S4: Top-1% and hypervolume profiles for Case 3 experiments comparing diversity-enhancing acquisition strategies (Section 3.3, Figure 6). All runs used PHI for acquisition. Results are shown for top- k batching without clustering and three diversity-enhanced acquisition strategies that apply clustering. Docking scores to IGF1R and CYP3A4 were minimized and maximized, respectively. The virtual library and docking scores were use as published in DOCKSTRING.^{S1} 1% of the virtual library was acquired at each iteration using top- k batching. Means \pm one standard deviation across 5 trials are shown.

Top-1%							
Cluster Type	0	1	2	Iteration 3	4	5	6
Feature	0.01 ± 0.00	0.04 ± 0.01	0.08 ± 0.02	0.12 ± 0.02	0.16 ± 0.02	0.19 ± 0.02	0.23 ± 0.02
Feature + Obj	0.01 ± 0.00	0.04 ± 0.01	0.07 ± 0.01	0.12 ± 0.02	0.16 ± 0.02	0.20 ± 0.02	0.24 ± 0.02
No clustering	0.01 ± 0.00	0.03 ± 0.01	0.07 ± 0.02	0.11 ± 0.03	0.17 ± 0.04	0.24 ± 0.04	0.28 ± 0.03
Obj	0.01 ± 0.00	0.03 ± 0.00	0.05 ± 0.01	0.09 ± 0.01	0.13 ± 0.01	0.17 ± 0.01	0.20 ± 0.01
Hypervolume							
Cluster Type	0	1	2	Iteration 3	4	5	6
Feature	0.72 ± 0.09	0.86 ± 0.07	0.97 ± 0.01	0.97 ± 0.01	0.98 ± 0.01	0.98 ± 0.01	0.99 ± 0.01
Feature + Obj	0.72 ± 0.09	0.87 ± 0.04	0.93 ± 0.04	0.96 ± 0.04	0.98 ± 0.02	1.00 ± 0.00	1.00 ± 0.00
No clustering	0.72 ± 0.09	0.81 ± 0.07	0.86 ± 0.10	0.90 ± 0.11	0.97 ± 0.03	0.97 ± 0.03	0.98 ± 0.03
Obj	0.72 ± 0.09	0.85 ± 0.06	0.94 ± 0.03	0.96 ± 0.04	0.98 ± 0.01	0.99 ± 0.01	0.99 ± 0.01

Table S5: Comparison of diversity-enhancing acquisition strategies using all four evaluation metrics after a fixed exploration budget of 6 iterations (Section 3.3, Figure 6). All runs used PHI for acquisition. Results are shown for top- k batching without clustering and three diversity-enhanced acquisition strategies that apply clustering. Docking scores to IGF1R and CYP3A4 were minimized and maximized, respectively. The virtual library and docking scores were use as published in DOCKSTRING.^{S1} 1% of the virtual library was acquired at each iteration using top- k batching. Means \pm one standard deviation across 5 trials are shown.

Cluster Type	Top 1%	Hypervolume	IGD	Fraction of True Front	Number of Scaffolds
Feature	0.23 ± 0.02	0.99 ± 0.01	0.26 ± 0.08	0.58 ± 0.07	10605 ± 146
Feature + Obj	0.24 ± 0.02	1.00 ± 0.00	0.09 ± 0.05	0.84 ± 0.05	9851 ± 49
No clustering	0.28 ± 0.03	0.98 ± 0.03	0.19 ± 0.15	0.72 ± 0.15	7946 ± 186
Obj	0.20 ± 0.01	0.99 ± 0.01	0.25 ± 0.08	0.64 ± 0.16	9036 ± 198

References

- (S1) García-Ortegón, M.; Simm, G. N. C.; Tripp, A. J.; Hernández-Lobato, J. M.; Bender, A.; Bacallado, S. DOCKSTRING: Easy Molecular Docking Yields Better Benchmarks for Ligand Design. *Journal of Chemical Information and Modeling* **2022**, *62*, 3486–3502.
- (S2) McInnes, L.; Healy, J.; Saul, N.; Großberger, L. UMAP: Uniform Manifold Approximation and Projection. *Journal of Open Source Software* **2018**, *3*, 861.
- (S3) Enamine Screening Collections. <https://enamine.net/compound-collections/screening-collection>.
- (S4) Adasme, M. F.; Linnemann, K. L.; Bolz, S. N.; Kaiser, F.; Salentin, S.; Haupt, V.; Schroeder, M. PLIP 2021: Expanding the Scope of the Protein–Ligand Interaction Profiler to DNA and RNA. *Nucleic Acids Research* **2021**, *49*, W530–W534.